APL Bioengineering ARTICLE pubs.aip.org/aip/apb

Degradation-aware neural imputation: Advancing decoding stability in brain machine interfaces

Cite as: APL Bioeng. **9**, 026106 (2025); doi: 10.1063/5.0250296
Submitted: 24 November 2024 · Accepted: 8 April 2025 ·
Published Online: 16 April 2025

Yun-Ting Kuo,[1] Han-Lin Wang,[1] Bo-Wei Chen,[1] Ching-Fu Wang,[1,2] Yu-Chun Lo,[3] Sheng-Huang Lin,[4,5] Po-Chuan Chen,[6] and You-Yin Chen[1,3,a)]

AFFILIATIONS

[1]Department of Biomedical Engineering, National Yang Ming Chiao Tung University, No. 155, Sec. 2, Linong St., Taipei 112304, Taiwan
[2]Biomedical Engineering Research and Development Center, National Yang Ming Chiao Tung University, No. 155, Sec. 2, Linong St., Taipei 112304, Taiwan
[3]Ph.D. Program in Medical Neuroscience, College of Medical Science and Technology, Taipei Medical University, 12F, Education & Research Building, Shuang-Ho Campus, No. 301, Yuantong Rd., New Taipei City 23564, Taiwan
[4]Department of Neurology, Hualien Tzu Chi Hospital, Buddhist Tzu Chi Medical Foundation, No. 707, Sec. 3, Zhongyang Rd., Hualien 97002, Taiwan
[5]Department of Neurology, School of Medicine, Tzu Chi University, No. 701, Sec. 3, Zhongyang Rd., Hualien 97004, Taiwan
[6]Department of Mechanical Engineering, University of Minnesota, Minneapolis, Minnesota 55455, USA

Note: This paper is part of the Special Topic on Bioengineering of the Brain.
[a)]**Author to whom correspondence should be addressed:** irradiance@so-net.net.tw

ABSTRACT

Neural signal degradation poses a significant challenge in maintaining stable performance when decoding motor tasks using multiunit activity (MUA) and local field potential (LFP) signals in the implantable brain machine interface (iBMI) applications. Effective methods for imputing degraded or missing signals are essential to restore neural signal integrity, thereby improving decoding accuracy and system robustness over long-term recordings with fluctuating signal quality. This study introduces a confidence-weighted Bayesian linear regression (CW-BLR) approach to impute neural signals affected by degradation, enhancing the robustness and consistency of decoding. The performance of CW-BLR was compared to traditional methods—mean imputation (Mean-imp) and Gaussian-mixture-model-based expectation–maximization (GMM-EM)—using a kernel-sliced inverse regression (kSIR) decoder to evaluate decoding outcomes. Four Wistar rats were trained to perform a forelimb-reaching task while neural activity (MUA and LFPs) was recorded over 27 days. CW-BLR imputed signals degraded during days 8–27. Decoding performance was evaluated using kSIR and compared with Mean-imp and GMM-EM. CW-BLR demonstrated superior performance by effectively preserving both temporal and spatial dependencies within the neural signals. CW-BLR-imputed data significantly improved decoding accuracy over traditional imputation methods, with the kSIR decoder showing consistently higher performance, particularly in maintaining signal quality from the degraded period. CW-BLR offers a robust and effective imputation framework for iBMI applications, addressing signal degradation challenges and maintaining accurate decoding over prolonged recordings. By utilizing confidence-based quality metrics, CW-BLR surpasses traditional methods, providing stable neural decoding across fluctuating signal quality scenarios.

I. INTRODUCTION

Implantable brain-machine interfaces (iBMIs) decode neural activity from implanted microelectrodes to control robotic devices. As these technologies advance toward clinical applications, addressing challenges related to the long-term usability and accuracy of neural signal decoding is crucial. Neural signals are primarily recorded using two modalities—spikes and local field potentials (LFPs)—each with unique strengths and limitations for sustained decoding. Spikes, derived from extracellular recordings, are categorized into single-unit activity (SUA), representing individual neurons, and multi-unit

activity (MUA), reflecting multiple neurons within the same channel.[1] By analyzing spike trains, these signals are translated into rate or timing codes, offering high temporal decoding accuracy.[2] In contrast, LFPs are low-frequency signals generated by the summation of postsynaptic potentials from neuronal populations.[3] Decoding LFP signals relies on features like oscillation patterns and spectral characteristics.[4] While LFPs provide lower temporal decoding accuracy than spikes due to broader frequency content, they demonstrate greater long-term stability.[4,5]

While combining spike and LFP signals as input features for decoders enhances decoding accuracy by leveraging complementary information,[6,7] the long-term performance of decoders deteriorates due to signal degradation.[8] Factors, such as micromotion and tissue reactions, exacerbate signal instability. Micromotion can alter the relative positions of neurons and implanted electrodes, leading to changes in neural recording conditions,[9] while inflammatory responses increase impedance at the electrode–tissue interface, distorting both spike and LFP signals.[10] These challenges necessitate strategies to counteract neural signal degradation to ensure consistent input features for decoders.

The degradation of recorded neural signal features over time renders pretrained decoder models impractical due to inconsistent input dimensions. Various methods have been proposed to maintain long-term decoding accuracy, such as filtering low-quality signal data and retraining models.[11] However, these approaches are time-intensive, rely on deteriorating data, and ultimately reduce model effectiveness and decoding accuracy.[12] Even with retraining, model performance continues to decline as input data quality diminishes, necessitating alternative strategies to address the underlying issues of signal degradation.

To counteract this decline, restoring degraded neural features from both spikes and LFPs has become essential. Two primary approaches to this problem are data alignment and data imputation. Data alignment methods, such as manifold realignment, address temporal or spatial discrepancies in the data,[13,14] ensuring consistency across recordings. While alignment improves data synchronization, it does not directly address signal degradation. Adaptive decoding algorithms, leveraging manifold realignment, maintain consistent decoder performance over time but fail to restore degraded signal quality.[13] In contrast, data imputation fills in missing or corrupted data points with estimated values, enhancing dataset completeness and improving neural decoding performance.

Among imputation methods, the mean imputation (Mean-imp) substitutes invalid data with the dataset's mean value, providing quick and efficient restoration.[15] However, Mean-imp disregards temporal structures and variable correlations dimension,[16] potentially distorting event-related information and reducing decoding accuracy.[17] Advanced methods like expectation–maximization (EM) improve imputation robustness by iteratively estimating parameters to address uncertainties in missing data.[18] Gaussian-mixture-model-based EM (GMM-EM) extends this approach by modeling data using Gaussian distributions, effectively restoring low-quality signals while preserving temporal patterns.[19] However, GMM-EM faces several challenges, including biases introduced by its reliance on Gaussian assumptions, overfitting due to excessive Gaussian components, and limitations from assuming variable independence. These shortcomings impede its ability to handle the complexities of neural signals, particularly when significant interdependencies exist.[20,21] Additionally, the computational demands of GMM-EM and its sensitivity to parameter initialization can hinder its practical application, while difficulties in achieving convergence may result in suboptimal imputation.[21,22]

To restore neural features efficiently, we introduce a noise-aware missing data imputation algorithm called confidence-weighted Bayesian linear regression (CW-BLR). This method restores sequences of binned MUA spike counts and binned LFP powers that may have deteriorated over time. CW-BLR imputes based on the quality metrics of the MUA signal-to-noise ratio (*SNR*) and LFP coherence (*Coh*), ensuring that the imputation process is sensitive to the quality of the data being restored. By incorporating confidence weights derived from these quality metrics into the regression framework, CW-BLR enables the effective reconstruction of missing or degraded data points during the imputation process.

This study aims to restore both MUA counts and LFP powers to their originally intended features. The maximal information coefficient (MIC) was used to confirm the correlation between neural features and the kinematics parameter of forelimb movement during repetitive reaching tasks. The MIC does not assume a specific pattern in the dataset and, thus, suits the detection of correlations in neural features. In this study, a neural decoder based on kernel-sliced inverse regression (kSIR) was developed and optimized through cross-validation using high-quality neural feature data collected from seven days of recordings (day 1 to day 7) to ensure decoding efficiency. MIC analysis was used to identify neural features that were strongly correlated with forelimb-reaching movements. From recording day 8 to day 27, CW-BLR was used to impute neural features from recording channels with degraded signal quality. For the performance evaluation of CW-BLR, actual and imputed neural features were used to decode animal forelimb movement trajectories, and its decoding robustness was examined using kSIR. Finally, we compared the long-term decoding performance of CW-BLR, Mean-imp, and GMM-EM using the imputed neural features.

II. RESULTS

A. Optimal tuning parameters of the kSIR model

In this study, the kSIR model was built using six levels of kernel width ($\sigma = 0.60, 0.70, 0.80, 0.90, 1.00, 1.1$) and six levels of regularization parameter ($r = 0.08, 0.09, 0.10, 0.11, 0.12, 0.13$) from the training set during the baseline period (days 1–7). A fivefold cross-validation approach was employed to identify the optimal σ and r pair that yielded the lowest RMSE for predicting forelimb movement velocities along the x- and y-axes. The heat map in Fig. 1 shows that the lowest RMSE (7.35 ± 1.09) was achieved when $\sigma = 0.9$ and $r = 0.10$, as represented by the white cell. This combination indicates the optimal tuning parameters for the kSIR decoder with an RBF kernel, providing the best decoding performance across the four animals.

The detailed performance for each pair of σ and r, along with statistical analysis results, is provided in Fig. S3 and Table S4 in the supplementary Note 4. These results confirm that $\sigma = 0.90$ and $r = 0.10$ significantly reduce the RMSE compared to other parameter combinations, ensuring a more robust and accurate neural decoding performance. Consequently, these optimal tuning parameters were selected for further neural decoding analyses.

B. Consistency of neural decoding with neurophysiological characteristics

Figure 2 illustrates the contribution ratio (% *CONTRIB*) of MUA features from eight channels and LFP power features from six frequency bands (δ, θ, α, β, γ, and γ') during the baseline period (recording days 1–7) for predicting forelimb x-velocity and y-velocity using a trained kSIR neural decoder. Our results show the contribution ratio for a specific rat (*Rat #4*, *#6*, *#9*, and *#10*) for either x-velocity [Fig. 2(a)] or y-velocity [Fig. 2(b)]. The contribution ratios of the MUA features are individually presented for each channel (labeled 1–8), while the contribution ratios of LFP power are aggregated for each frequency band across all eight channels. The results indicate that MUA features from each channel contribute more significantly to the kSIR model's prediction of both x- and y-velocity compared to LFP power features. Among the LFP frequency bands, the γ and γ' bands show higher contribution ratios, indicating that these high-frequency LFP bands are more relevant for predicting forelimb movements compared to lower frequency bands, such as δ, θ, α, and β. This trend is consistent across all four rats, emphasizing the importance of MUA and high-frequency LFP bands in capturing movement dynamics during the baseline period. The consistent contribution of MUA features and the high relevance of LFP γ and γ' bands highlight their critical roles in accurately modeling and predicting forelimb movement trajectories.

Figure 3 showed the MIC values for MUA are the highest among all neural features, demonstrating the strongest correlation with forelimb-reaching movements, followed by LFP γ and γ' frequency bands. These results suggest that MUA, along with LFP γ and γ' bands, possess strong predictive power for capturing movement dynamics. The other LFP frequency bands, including δ, θ, α, and β, show relatively low MIC values, indicating weaker correlations with forelimb movement velocities. This trend is consistent for both x- and y-velocity components, emphasizing the importance of MUA and high-frequency LFP bands in encoding movement-related information.

These observations align with the results from the MIC analysis (Fig. 3), where the sequence of binned MUA firing counts and LFP power from the γ and γ' bands contributed most significantly to the kSIR decoding of forelimb movements, more so than the LFP power from lower frequency bands. The MIC analysis highlighted the high correlation between MUA and high-frequency LFP bands (γ and γ') with movement velocities, confirming their predictive power in capturing forelimb dynamics. This consistency in neural feature contributions observed in the kSIR decoding model (Fig. 2) and their strong correlations with forelimb movements further validates the ability of kSIR to effectively utilize these neural features to predict forelimb movement trajectories. The decoder capitalizes on the neurophysiological properties of MUA and high-frequency LFP bands, which are closely related to motor control, ensuring accurate predictions of movement trajectories over time. This robust relationship between feature contribution and movement correlation underscores the importance of MUA and high-frequency LFP bands in motor-related neural decoding tasks.

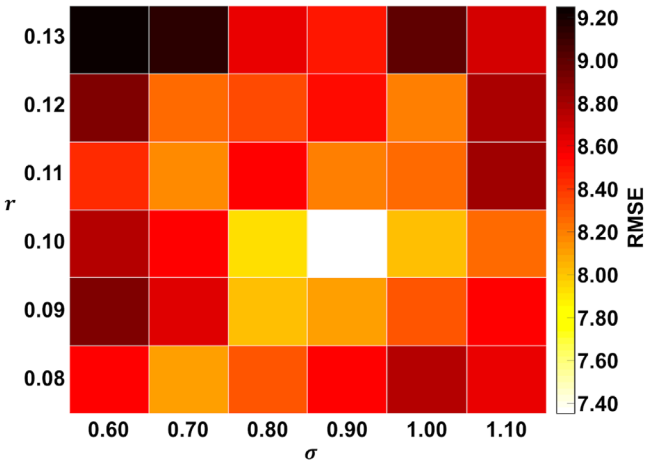

FIG. 1. Heat map showing the decoding performance of the kSIR model for different combinations of kernel width (σ) and regularization parameter (r) using RMSE as the evaluation metric. Each cell in the heat map represents the average RMSE value for a specific pair of σ and r, with warmer colors (e.g., red and dark brown) indicating higher RMSE values (worse performance) and cooler colors (e.g., yellow and white) indicating lower RMSE values (better performance). The RMSE values range from 7.8 to 9.0, as indicated by the color scale on the right. The kSIR model was built using six levels of σ (0.60, 0.70, 0.80, 0.90, 1.00, 1.10) and six levels of r (0.08, 0.09, 0.10, 0.11, 0.12, 0.13) during the baseline period (days 1–7) for each animal, and the optimal combination of $\sigma = 0.9$ and $r = 0.10$ yielded the lowest RMSE (7.72 ± 0.62), as shown by the white cell in the heat map. This pair of tuning parameters was selected as the optimal setting for the kSIR model in subsequent neural decoding analyses.

C. Restoring neural features with CW-BLR enhancement of long-term decoding robustness

Figure 4 illustrates the comparison of decoding performance for forelimb movement trajectories between the non-imputed and CW-BLR-imputed neural features from the 8th to the 27th recording day. Figure 4(a) presents a visual interpretation of the predicted forelimb trajectories using the kSIR decoder based on non-imputed and CW-BLR-imputed neural features compared to the actual trajectories across different days. The predicted trajectories using CW-BLR-imputed features align closely with the actual forelimb movement trajectories, especially from day 8 to day 16, indicating that the imputed neural features maintain high fidelity in capturing the true movement dynamics. In contrast, trajectories predicted using non-imputed features show greater deviations from the actual trajectories, particularly from day 18 onward, reflecting a decline in signal quality and decoding accuracy as recording days progress.

Figures 4(b) and 4(c) show the RMSEs of the predicted forelimb trajectories along the x-axis and y-axis, respectively, for the non-imputed and CW-BLR-imputed features over the 27-day recording period. From the 8th to the 27th recording day, the RMSE values for both x- and y-axes gradually increase as signal quality degrades. However, CW-BLR-imputed features exhibit significantly lower RMSE values than non-imputed features from the 16th to the 27th day ($p < 0.05$), indicating that the CW-BLR method effectively restores neural features and maintains decoding robustness even as recording quality deteriorates. This trend is particularly evident on day 27, where the imputed channel ratio exceeds 50%, suggesting substantial signal degradation. Despite this, the CW-BLR method outperforms non-imputed features, demonstrating its capability to handle severe signal quality degradation.

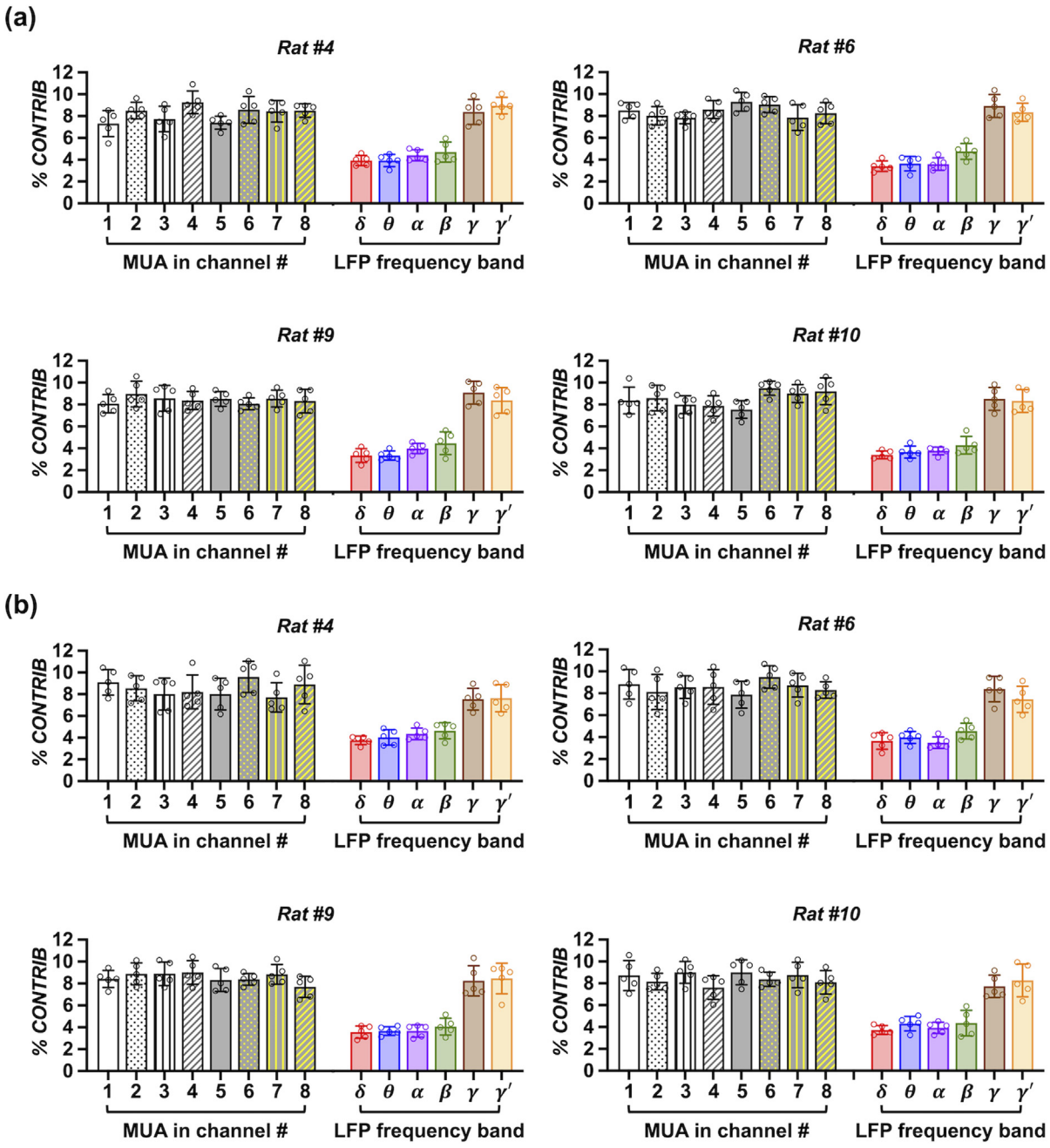

FIG. 2. Contribution ratio (% *Contribution*) of MUA and LFP features in predicting forelimb movement velocities along the x- and y-axes during the baseline period (recording days 1–7). (a) Contribution ratios of neural features for predicting forelimb movement velocity along the x-axis. (b) Contribution ratios of neural features for predicting forelimb movement velocity along the y-axis. Each subplot displays the % Contribution of MUA and LFP features for a specific rat (*Rat #4*, *#6*, *#9*, and *#10*) using the kSIR neural decoder. The contribution ratios of MUA features are shown individually for each channel (labeled 1–8), while the contribution ratios of LFP features are accumulated for each frequency band (δ, θ, α, β, γ, and γ') across all channels. MUA features from each channel show the highest contribution in predicting both x- and y-velocity components compared to LFP power. Among the LFP frequency bands, the γ and γ' and exhibit higher contribution ratios, indicating their relevance in decoding forelimb movements. Data are presented as mean ± SD.

Overall, the results in Fig. 4 confirm that the CW-BLR method can substantially improve the robustness and accuracy of decoding performance compared to non-imputed neural features under conditions of declining signal quality. Although the effectiveness of CW-BLR gradually diminishes as the imputed channel ratio increases beyond 50% on day 27, it still achieves more reliable movement trajectory predictions than the non-imputed approach. This underscores the utility of CW-BLR in maintaining stable neural decoding performance

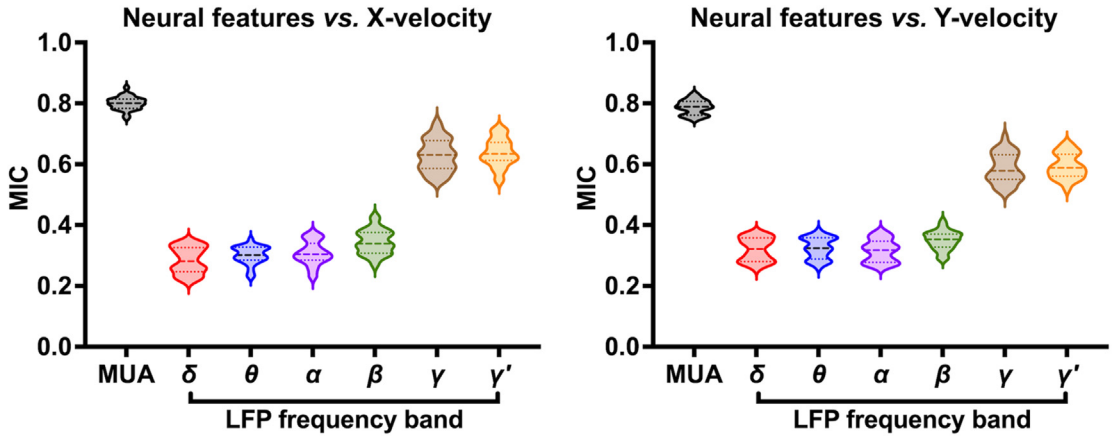

FIG. 3. Correlation between neural feature and forelimb-reaching movement. The correlation results of using the MIC method to quantify the functional relationship between input neural features and actual forelimb movement velocities along the x-axis (left) and y-axis (right) during a forelimb-reaching task. Data shown are averaged from the baseline period (recording days 1–7) and across four animals. This result shows that MUA, along with high-frequency LFP bands, have strong predictive power in capturing movement dynamics. The MICs of MUA and LFP six frequency bands were visualized as violin plot. Data provide baseline correlations, whereas changes in the correlation between neural features and kinematic parameters (forelimb movement velocities) over 27 days are presented in the Fig. S4 of supplementary Note 5.

over prolonged recording periods, despite significant changes in neural recording conditions.

D. Computational performance and decoding accuracy: CW-BLR vs GMM-EM and Mean-imp

Table I presents the computational complexity and execution time of CW-BLR, GMM-EM, and Mean-imp for a single binned neural feature as well as a combined set of binned MUA firing counts and binned LFP power. The computational complexity of CW-BLR is $O(n^3)$, where n represents the number of input neural features ($n = 8$ for binned MUA firing counts; $n = 6 \times 8$ for binned LFP power). This reflects CW-BLR's higher computational demand due to its Bayesian linear regression framework. In contrast, GMM-EM has a complexity of $O(n^2)$, while Mean-imp is significantly less complex at $O(1)$. Despite its higher complexity, the average execution time for CW-BLR was 1.30 ± 0.23 ms for MUA firing counts and 1.48 ± 0.25 ms for LFP power, resulting in a combined execution time of 2.55 ± 0.20 ms per bin. While GMM-EM showed faster performance with an average combined time of 1.83 ± 0.26 ms, Mean-imp was the most efficient at 0.65 ± 0.08 ms. However, statistical analysis using the Kruskal–Wallis test indicated a significant difference between CW-BLR and Mean-imp ($p < 0.05$). These results demonstrate that while CW-BLR requires more computational resources than Mean-imp and GMM-EM, it maintains an acceptable execution time for real-time neural decoding applications.

Following the confirmation that the restoration of neural features through CW-BLR enhanced decoding robustness, we compared the decoding accuracy of forelimb trajectories using neural features restored by CW-BLR with those restored by GMM-EM and Mean-imp. Figure 5(a) presents the predicted forelimb movement trajectories along the x- and y-axes using the kSIR decoder based on neural features restored by CW-BLR, GMM-EM, and Mean-imp methods, compared to the actual movement trajectories (black dashed line). The predictions are shown for several key recording days (day 8, 10, 12, 14, 16, 18, 20, 22, 24, and 27), illustrating how closely each imputation method can reconstruct the forelimb trajectories as recording days progress. Among the three methods, CW-BLR-imputed features exhibit the closest alignment with the actual forelimb movement trajectories across all recording days, particularly from the 8th to 16th recording day, demonstrating higher accuracy and stability in trajectory prediction. GMM-EM-imputed features show a moderate alignment with actual trajectories, while Mean-imp-imputed features deviate significantly from the actual trajectories, particularly from day 18 onward, indicating a decline in predictive performance as signal quality deteriorates.

Figure 5(b) compares RMSEs of the predicted forelimb trajectories along the x-axis for the CW-BLR-imputed, GMM-EM-imputed, and Mean-imp-imputed features from the 8th to the 27th recording day. During the early recording period (from 8th to 14th recording day), all three methods show relatively low RMSE values, indicating good alignment with actual trajectories. As the recording period progresses, the RMSE values for all three methods increase, reflecting the challenges in maintaining decoding accuracy under deteriorating signal quality. However, CW-BLR consistently achieves lower RMSE values compared to GMM-EM and Mean-imp, particularly from the 16th recording day onward ($p < 0.05$). This indicates that CW-BLR can better preserve the accuracy of decoded forelimb trajectories under conditions of signal degradation. In contrast, GMM-EM and Mean-imp show a faster increase in RMSE values, especially on the 27th recording day, suggesting their reduced capability in handling severe signal quality deterioration.

Figure 5(c) shows the RMSE values for predicted forelimb trajectories along the y-axis for the three imputation methods over the 27 recording days. Similar to the results along the x-axis, CW-BLR maintains significantly lower RMSE values compared to GMM-EM and Mean-imp, particularly from the 16th to 27th recording day. As the imputed channel ratio increases over time and exceeds 50% on the 27th recording day, the effectiveness of GMM-EM and Mean-imp diminishes rapidly, resulting in significantly higher RMSE values. Despite the increasing imputed channel ratio, CW-BLR outperforms

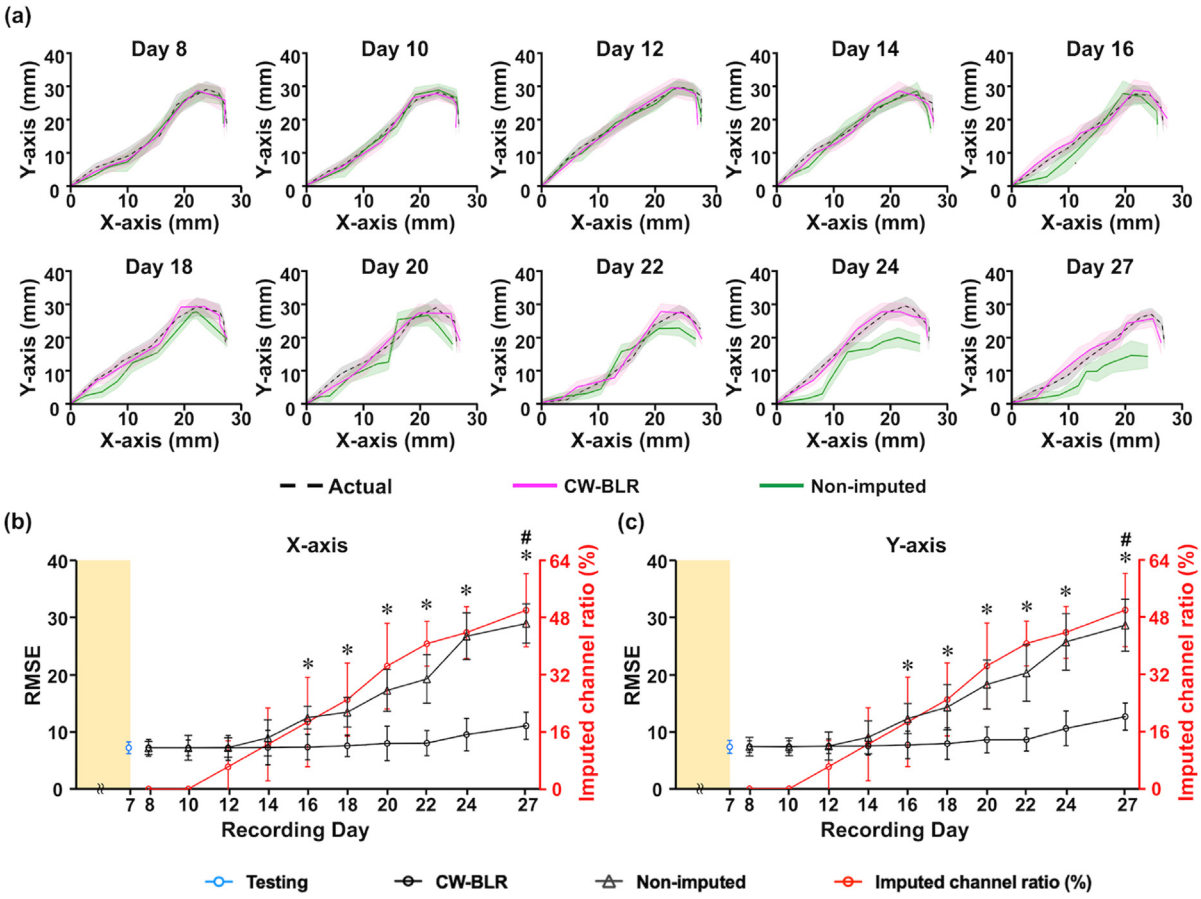

FIG. 4. Comparison of forelimb movement trajectory decoding performance between non-imputed and CW-BLR-imputed neural features from the 8th to the 27th recording day. (a) Predicted forelimb trajectories based on the kSIR decoder using CW-BLR-imputed neural features (magenta) show a closer alignment with the actual movement trajectories (black dashed line) compared to non-imputed features (green) across multiple recording days. (b) and (c) display the RMSE of trajectory decoding along the x-axis and y-axis, respectively, over the 27 recording days. CW-BLR-imputed features demonstrate significantly lower RMSE values than non-imputed features from the 16th to the 27th recording day (Friedman test followed by Dunn–Bonferroni *post hoc* test, $*p < 0.05$), reflecting more accurate predictions despite signal quality deterioration. The imputed channel ratio (red line) indicates the proportion of channels requiring imputation due to degraded signal quality. As the imputed channel ratio increases and exceeds 50% on day 27, the stability of CW-BLR-imputed decoding performance decreases, although it still outperforms the non-imputed method. The symbol # denoted decoders driven by CW-BLR-imputed neural features on the 27th recording day whose RMSE values significantly higher (Wilcoxon signed-rank test, $^{\#}p < 0.05$) than the RMSE obtained from decoding using testing dataset of the baseline period (days 1–7). The yellow-shaded region represents the baseline period (days 1–7). Data are presented as mean ± SD from *Rat #4*, *Rat #6*, *Rat #9*, and *Rat #10*.

TABLE I. Computational complexity and corresponding execution time of CW-BLR, GMM-EM, and Mean-imp.

Imputation methods	Computational complexity	Average execution time[a] of imputation for neural feature per bin		
		MUA firing counts[b]	LFP power[b]	MUA firing counts + LFP power[b]
CW-BLR	$O(n^3)$	1.30 ± 0.23 ms	1.48 ± 0.25 ms	2.55 ± 0.20 ms
GMM-EM	$O(n^2)$	0.91 ± 0.27 ms	1.02 ± 0.21 ms	1.83 ± 0.26 ms
Mean-imp	$O(1)$	0.32 ± 0.10 ms	0.35 ± 0.18 ms	0.65 ± 0.08 ms[c]

[a]The 285 binned neural features to be imputed. Data are presented as mean ± SD.
[b]MATLAB-coding CW-BLR, GMM-EM, and Mean-imp performed the neural feature imputations on the hardware setup of Intel(R) Core (TM) i9-9900K CPU @ 3.60 GHz with 32 GB RAM.
[c]Significant difference when compared to CW-BLR ($p < 0.05$) by using the Kruskal–Wallis test.

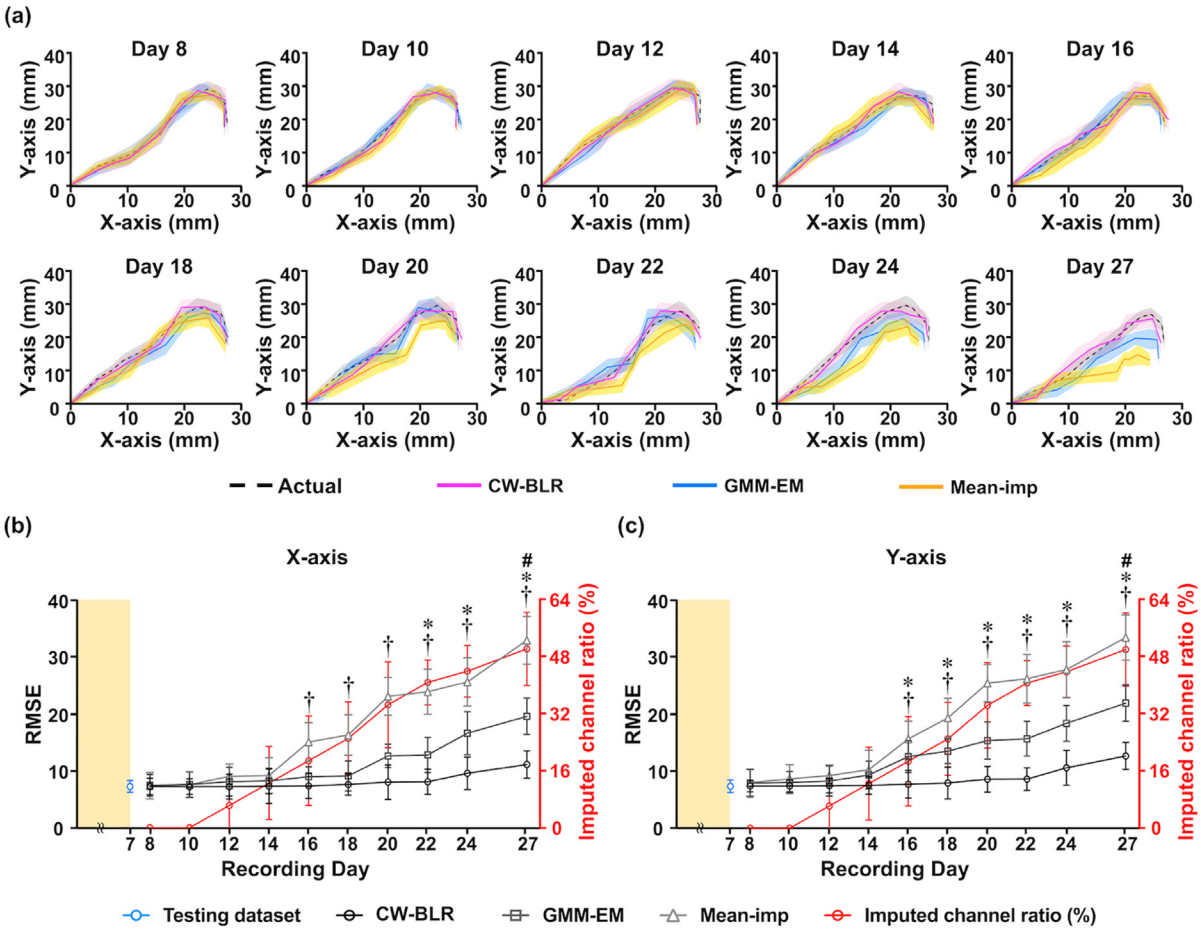

FIG. 5. Comparison of forelimb trajectory decoding performance using neural features restored by CW-BLR, GMM-EM, and Mean-imp from the 8th to the 27th recording day. (a) Predicted forelimb trajectories along the x- and y-axes using the kSIR decoder based on neural features restored by CW-BLR (magenta line), GMM-EM (blue line), and Mean-imp (orange line) methods compared to actual forelimb trajectories (black dashed line) for several key recording days. Data shown are averaged from four animals and the shadow regions represented the corresponding SD for the deviation of predicted trajectories. CW-BLR-imputed features show the closest alignment with actual forelimb trajectories, while GMM-EM and Mean-imp-imputed features exhibit greater deviations, particularly in later recording days. (b) and (c) show the RMSEs (left axis) of predicted forelimb trajectories along the x-axis and y-axis, respectively, for the three imputation methods over 27 recording days. the right axis represented the imputed channel ratio (%). CW-BLR-imputed features maintain significantly lower RMSE values compared to GMM-EM and Mean-imp, especially from 16th recording day to 27th recording day, demonstrating greater decoding robustness and accuracy under deteriorating signal conditions. The symbol $*$ indicated the neural features imputed by GMM-EM whose RMSE vales significantly higher than that imputed by CW-BLR (Friedman test followed by Dunn–Bonferroni post hoc test, $^{*}p < 0.00167$). The symbol † indicated the neural features imputed by Mean-imp whose RMSE values significantly higher than that imputed by CW-BLR (Friedman test followed by Dunn–Bonferroni post hoc test, $^{\dagger}p < 0.00167$). The symbol # denoted decoders driven by CW-BLR imputed neural features on the 27th recording day whose RMSE vale significantly higher (Wilcoxon signed-rank test, $^{\#}p < 0.05$) than the RMSE (blue-hollow circle) obtained from kSIR decoding using testing dataset of the baseline period (days 1–7). The imputed channel ratio (red line) increases over time as signal quality degrades, exceeding 50% on the 27th recording day. Despite this, CW-BLR outperforms the other two methods, highlighting its superior capability in handling severe signal degradation and maintaining accurate forelimb trajectory predictions. Data are presented as mean ± SD from *Rat #4*, *Rat #6*, *Rat #9*, and *Rat #10*.

the other two methods, demonstrating its robustness and superior ability to maintain accurate forelimb trajectory predictions even under severe signal degradation. This comparison confirms that the superior performance of CW-BLR over GMM-EM and Mean-imp highlights its effectiveness in restoring degraded neural features and ensuring reliable movement trajectory predictions despite the challenges posed by long-term recording conditions. This robustness makes CW-BLR a suitable method for maintaining stable neural decoding performance over extended periods with substantial variations in signal quality.

III. DISCUSSION

A. Explainability analysis of neural feature contributions to kSIR-based decoding

The investigation of the neural feature weight distribution of the trained kSIR model, particularly in the context of forelimb movement, provides critical insight into the neural dynamics associated with motor behavior. By comparing the weight distribution of features, such as MUA firing counts and the LFP spectral power across various frequency bands, we elucidate how these neural features contribute to

movement decoding. This explainability analysis is conducted to enhance our understanding of the model's performance and obtain a framework for assessing its biological plausibility.[23]

In the context of forelimb-reaching tasks, our study demonstrates a significant MIC correlation between the MUA firing counts and kinematic parameters in M1. This emphasizes the strong link between M1 neural activity and motor behavior, suggesting that MUA firing counts are a potential control signal for contemporary iBMIs.[24] M1 neuron activation during forelimb movements indicates the execution of motor tasks,[25] where M1 directly influences muscle contractions through its projections to the spinal cord. Repetitive forelimb movements lead to adaptive changes in neural activity patterns within M1, establishing a specific neural representation that corresponds to the executed motion. The kSIR model effectively leverages these neural dynamics by assigning higher weights to MUA features, highlighting their critical role in capturing forelimb movement trajectories.

The high MIC correlations observed between specific LFP frequency bands and kinematic parameters corroborate previous studies[26,27] that linked afferent proprioceptive feedback to LFP γ (30–100 Hz) oscillations during movement.[28] The LFP spectral power in the γ band is associated with sensory systems and cognitive processes during motor control.[29,30] Proprioceptive information is projected to M1 via muscle spindle afferents, which connect the nucleus ventroposterior lateralis of the thalamus to M1.[31] This indirect pathway enables sensorimotor rhythms to integrate motor information with M1,[32] thus supporting motor execution. Frequencies above 30 Hz, which reflect spike activity during voluntary movements in M1,[33] capture the average effect of postsynaptic potentials surrounding the electrode, indicating the reaction of spiking activity to kinematic changes.[34] This suggests that the LFP γ and γ' bands, similar to MUA spike counts,[35] encode essential motor information,[9] which are assigned large weights by the kSIR model in decoding.[36]

Low-frequency LFP bands, particularly the α band (8–12 Hz) and β band (13–30 Hz), are generally extensively linked to various aspects of motor control, sensorimotor integration, and movement planning.[37–39] The LFP α band is often associated with relaxation and inhibition,[40] whereas the LFP β band plays a role in movement initiation and inhibition, reflecting the brain's preparatory processes for motor actions.[41] However, recent studies highlight the importance of high-frequency bands, specifically γ and γ' oscillations, in the context of motor execution and the fine-tuning of actions.[29,42] These higher-frequency oscillations correlate more closely with the actual execution of movements, suggesting a shift in the understanding of the functional roles of different frequency bands in motor behavior. The LFP γ and γ' bands reflect the firing rates of local neuronal populations,[43,44] establishing a direct relationship between neural output and motor behavior. This relationship is significant because it underscores the role of these high-frequency oscillations in capturing neural processing dynamics during movement. The findings indicate that the power of the LFPs in the γ and γ' bands contribute more significantly to movement decoding accuracy than the lower-frequency bands, such as α and β. Therefore, high-frequency bands are more adept at capturing the rapid, transient neural dynamics associated with motor execution, which are critical for precise movement control. We further explore this phenomenon by comparing the contributions of different LFP frequency bands to the accuracy of forelimb movement decoding. The results demonstrate that the LFP powers in the γ and γ' bands are significantly more influential in enhancing the decoding accuracy compared with those in the lower-frequency bands. This finding reflects the importance of high-frequency oscillations for representing fast, transient neural dynamics and population-level synchronization, which are crucial for effective motor control. The superior performance of the γ and γ' bands in decoding movement velocities is attributed to their sensitivity to the synchronous firing of local neuron populations, which is vital for translating neural activity into coherent motor outputs. Moreover, the role of γ and γ' oscillations extends beyond mere representation of movement execution;[45] they facilitate interneuronal communication and local information processing,[46,47] which are critical for the timing and coordination required for rapid movements. This enhanced neuron communication may explain why these high-frequency LFP bands are more effective in decoding movement velocities,[48,49] as they encapsulate both the temporal and spatial aspects of neural communication and muscle activation patterns. The intricate interplay between these oscillations and motor behavior suggests that understanding the dynamics of γ and γ' oscillations can provide deeper insight into the neural mechanisms underlying motor control.

The observed high correlation between neural features and forelimb movements is consistent with the proportional weights assigned to these features in the kSIR model. This confirms the credibility of the kSIR model in decoding neural signals, enhancing the reliability and validity of the forelimb trajectory predictions. According to our explainability analysis, the kSIR model accurately captures the interaction between motor-related neural activity and corresponding behaviors and is, thus, an effective tool for understanding and predicting motor control. By examining the contribution of each feature to the kSIR model, we gain a comprehensive understanding of how MUA and LFP dynamics translate into forelimb movements, ultimately improving the model's interpretability and application in motor neuroscience research.[50,51]

B. Enhancing decoding robustness using CW-BLR considering MUA–LFP correlation

The integration of MUA and LFP signals is a significant advancement in addressing the limitations associated with using either feature independently. MUA provides high temporal resolution, which is crucial for capturing rapid neuronal dynamics; however, it is often compromised by noise sensitivity and biocompatibility issues. These factors can gradually compromise signal quality due to neuronal loss and tissue encapsulation over time, thereby undermining the reliability of feature extraction.[52,53] Although LFPs are more stable and less susceptible to noise, they frequently lack the temporal resolution necessary to capture the fine details of rapid changes in neuronal activity,[4,54,55] which are essential during dynamic motor tasks. Combining these two signal types through hybrid decoders leverages MUA's temporal precision alongside the spatial stability and contextual information provided by LFPs, ultimately enhancing movement decoding accuracy.[4,56]

Although the combination of MUA and LFP signals is beneficial, the long-term stability of both signal types declines over time,[57–59] which poses challenges for maintaining consistent decoding performance. The LFP band power, particularly in the higher-frequency ranges (such as γ and γ'), and MUA often diminish when recorded using conventional electrodes or advanced multichannel arrays, as

observed in the current and previous studies.[57,58] This deterioration in signal quality is likely due to the degradation of electrode coatings,[60] which reduces electrical conductivity[4] or increases the tissue–electrode impedance. The latter issue, caused by the tissue encapsulation of the implanted electrodes, results in a pronounced low-pass filtering effect, further compromising the reliability of long-term recordings. Consequently, when the quality of MUA and LFP signals falls below the levels established during the initial training of the neural decoders, the decoding performance can suffer significantly. This situation underscores the urgent need for robust methodologies that preserve signal integrity over time.

Our proposed CW-BLR is a critical tool for the simultaneous imputation of MUA and LFP signals. CW-BLR effectively reconstructs missing or corrupted data, thereby providing robust estimations of neural features and compensating for signal loss and degradation. By maintaining the integrity and consistency of both MUA and LFP signals, CW-BLR enables neural decoders to operate at high performance levels, even with fluctuations in signal quality. This ensures that hybrid decoders can continue to leverage the strengths of both signal types, thus sustaining decoding accuracy over extended periods.

One of the distinguishing features of CW-BLR is its robustness to noise and its ability to preserve the temporal dependencies within neural data. Traditional imputation methods, such as Mean-imp and regression-based techniques, often fail to account for the variability introduced by noise into neural signals. For instance, Mean-imp simplifies the imputation process by replacing missing values with the mean of the observed data,[61] which can distort the data's variability and temporal structure. Regression methods typically rely on linear assumptions between variables, making them vulnerable to biased estimates when actual relationships are nonlinear or when the data are noisy. In the context of neural signals, such as MUA firing counts and LFP powers, which exhibit temporal structures that vary with the executed motor behavior,[62] this structure should be maintained during imputation. CW-BLR addresses these limitations by integrating a probabilistic framework that incorporates confidence weights based on signal quality metrics (MUA *SNR* and LFP *Coh*). By dynamically adjusting these weights, CW-BLR effectively mitigates the influence of low-quality data, thereby reducing the risk of overfitting and preserving the temporal patterns inherent in neural signals.

CW-BLR considers the statistical distribution of currently recorded MUA firing counts while incorporating statistical data from adjacent time bins for both MUA firing counts and the LFP power across frequency bands. This approach captures the dependencies between the current and neighboring data; this is needed to maintain the temporal continuity of neural signals, which is essential for accurate trajectory decoding. Additionally, because data from neighboring recording channels are included in the imputation calculations, the imputed neural features reflect spatial variations or influences related to microelectrode implantation. Combined with temporal consistency, this spatial consideration ensures that the imputed data accurately represent the true dynamics of neural activity.

Unlike machine learning–based methods, such as k-nearest neighbor (KNN)[63] and decision tree algorithms,[64] which are effective for nonlinear data structures but struggle with temporal dependencies, CW-BLR leverages a Bayesian framework that explicitly models the uncertainty in missing or degraded data values. For example, KNN imputes missing values by averaging the values of the nearest neighbors, which can be computationally expensive in high-dimensional settings and may lead to biased estimates in cases with poorly defined neighborhoods. Decision trees, albeit adept at capturing nonlinear relationships, often overfit in noisy environments and are not inherently designed to model temporal dependencies or uncertainty in data. CW-BLR improves these methods by accounting for both linear and nonlinear relationships between variables while integrating confidence weighting, which adjusts the influence of each data point based on its signal quality. This confidence-weighted approach, combined with Bayesian regression, allows CW-BLR to capture the complexity of neural signals while maintaining robustness to noise and variability.

EM-based methods, such as GMM-EM, can restore time-series data and maintain some temporal structure,[65] but they often neglect the relationship between MUA firing counts and LFP powers, thereby compromising the temporal integrity of the imputed neural features. As the amount of missing information increases, GMM-EM requires more training samples to maintain imputation accuracy, leading to high variability in the imputed data.[66] Furthermore, GMM-EM's reliance on recalculating the likelihood function in every imputation step often results in convergence to different local maxima,[67] reducing its tolerance for imputed neural feature ratios compared with that of CW-BLR. This limitation becomes pronounced in cases with small sample sizes,[68,69] such as the less time bin covariance matrix used in this study, degrading GMM-EM's performance in restoring neural data.

Deep learning models are computationally intensive and require extensive training, so they are difficult to use when data characteristics shift or when underlying patterns are underrepresented.[70] This challenge is evident in neural recordings, where data quality fluctuates due to tissue reactions and environmental influences.717 CW-BLR adapts dynamically by incorporating prior knowledge and signal quality metrics (MUA *SNR* and LFP *Coh*), ensuring stable performance even with variable data quality.[9]

Compared with deep learning-based methods, CW-BLR excels in low-quality MUA and LFP signal imputation. Deep learning models require large, high-quality datasets, and decline in accuracy in cases with noisy, low-dimensional neural signals.[72] These models also demand extensive tuning or rely on pretrained architectures, increasing the risk of overfitting when data quality varies.[72] CW-BLR overcomes these issues by integrating the above-mentioned signal quality metrics into its confidence-weighted approach, enabling robust imputation even in sparse datasets.[9]

Deep learning models often cannot capture dependencies between neural features in low-quality data. By leveraging temporal and spatial correlations between MUA firing counts and LFP powers, CW-BLR preserves both neural dynamics and signal structures.[9] Hence, the proposed method restores degraded neural signals with higher fidelity, maintaining critical MUA–LFP relationships and improving the long-term decoding performance in iBMIs.[71] Deep learning's computational demands hinder real-time applications, where rapid responses are crucial.[70] By contrast, CW-BLR's adaptability allows it to adjust imputation strategies in real time, so it is ideal for time-sensitive fields, such as neuroprosthetics.[9] Additionally, CW-BLR's use of transparent, established signal quality metrics enhances interpretability, offering clear insights into its decision-making process, a critical advantage in clinical settings.[71]

By incorporating signal quality assessments, CW-BLR prioritizes low-quality neural recordings for imputation, enhancing overall decoding performance, unlike deep learning models, which may amplify noise without such assessments.[72] CW-BLR's ability to maintain temporal and spatial signal integrity is advantageous for BMIs, where accurate interpretation of neural signals is crucial for device control.[71] Hence, CW-BLR is an effective, reliable solution in BMI applications, particularly in communication or control scenarios where signal quality directly impacts usability.[71]

C. Limitations

CW-BLR is highly effective at imputing degraded neural signals and maintaining decoding accuracy. However, it is important to recognize that the method has certain limitations. To systematically evaluate the impact of increasing imputed channel ratios on decoding performance, we conducted a simulation using high-quality datasets recorded during the first seven days of the experiment. The simulation results (Fig. S5 in the supplementary Note 6) demonstrate that CW-BLR effectively restores neural features, enabling stable decoding performance even at higher imputation levels compared to GMM-EM and Mean-imp. These findings also align with Fig. 5, confirming that while all imputation methods lead to some performance degradation as the imputed channel ratio increases, CW-BLR demonstrates the highest tolerance for missing data. This resilience makes CW-BLR-imputed neural features superior to those generated by alternative methods in preserving decoding accuracy under conditions of neural signal degradation.

As the imputed channel ratio increases, a progressively larger portion of the dataset consists of reconstructed rather than actual recorded neural activity, leading to a reduction in neural feature variability—a critical factor for precise movement decoding. Variability in neural activity is essential for accurately encoding motor commands necessary for movement execution.[73–75] CW-BLR estimates missing neural features by leveraging spatial dependencies (signals from neighboring channels) and temporal dependencies (signals from adjacent time bins) to generate the most suitable imputed values. However, as more channels require imputation, the reconstructed data become overly reliant on adjacent signals, leading to artificially smoothed neural activity patterns.[76] This smoothing effect reduces signal distinctiveness, weakening the decoder's ability to separate meaningful motor-related activity from background noise, ultimately degrading decoding accuracy.[77,78]

Furthermore, excessive imputation disrupts the natural spatial and temporal distribution of neural features, further complicating decoding performance. In a well-structured neural dataset, distinct and dynamic signal patterns emerge across both time and space, reflecting the complexity of motor-related neuronal activity.[79] However, as imputation levels increase, reconstructed signals become excessively similar to neighboring data points, blurring the natural contrasts that characterize authentic neural activity. This loss of distinctiveness is particularly problematic in movement decoding, where subtle variations in neural signals are crucial for accurately distinguishing between different motor outputs. Consequently, while CW-BLR remains effective under moderate imputation levels, decoding performance declines sharply once the proportion of missing data surpasses a critical threshold.[76]

IV. CONCLUSION

Restoring neural features through imputation is crucial for maintaining long-term decoding accuracy in iBMIs and can significantly extend the lifespan of decoder training models. As a simple yet effective multivariate imputation method, CW-BLR is a promising solution for restoring neural features, particularly in time-dependent, correlated datasets, such as MUA firing counts and LFP powers. CW-BLR enhances the quality of neural decoding without model retraining, making it highly adaptable and efficient for use in long-term neural signal decoding. By using signal quality metrics (MUA *SNR* and LFP *Coh*) and considering the temporal and spatial dependencies of neural signals, CW-BLR preserves the integrity of neural dynamics during imputation. However, despite its robustness for moderate levels of missing data, the performance of CW-BLR diminishes when the ratio of imputed channels exceeds 50%, indicating the need for further optimization in such scenarios. Nevertheless, its capability to restore neural signals without repeated training and its adaptability to signal quality fluctuations make CW-BLR a valuable tool for iBMIs. It can address similar challenges in other applications, helping increase efficiency and stability in neural decoding systems over extended periods.

V. METHODS

A. Animals and experimental design

Ten male Wistar rats, weighing approximately 250–300 g, were purchased from BioLASCO, Taiwan Co., Ltd. The animals were housed in a temperature-controlled room under a 12-h inverted light/dark cycle with unrestricted access to food and water at the Taipei Medical University animal center. All animal care and handling procedures were approved by the Institutional Animal Care and Use Committee of Taipei Medical University (IACUC Approval number: LAC-2022-0207) in compliance with institutional guidelines and the 3R principles.

The experimental design involved training the rats on a skilled forelimb reach task for up to one week. Rats that successfully performed the lever-pressing task for three consecutive training days underwent surgery to implant microelectrodes in the primary motor cortex (M1) contralateral to their right forelimb. After a one-week recovery period, electrophysiological recordings and forelimb movement trajectory captures were conducted during reach tasks for seven consecutive days. This initial recording period (1st to 7th days) provided a robust training dataset for the neural decoder, capturing a diverse range of neural activity patterns under consistent conditions.

Initially, ten rats were included in the experiment. However, only four (identified as Rat #4, Rat #6, Rat #9, and Rat #10) completed the full 27 days of continuous neural signal recording following microelectrode implantation. In the remaining six animals (identified as Rat #1, Rat #2, Rat #3, Rat #5, Rat #7, Rat #8, and Rat #10), the microelectrodes either detached from the brain or the connectors were damaged due to unknown causes, necessitating the suspension of their corresponding neural recordings. These animals were excluded from the study.

For the remaining four rats (Rat #4, Rat #6, Rat #9, and Rat #10), long-term neural recordings from the 8th to the 27th recording days revealed variations in signal quality caused by changes in the implanted microelectrodes. These fluctuations disrupted the functional mapping between neural activity and kinematic parameters, reflecting the inherent challenges of maintaining stable neural signals in chronic

recordings. Our proposed imputation method was employed to evaluate its effectiveness in restoring the fluctuating neural features in the chronic recordings, preserving the temporal dynamics of neural activity and enhancing the robustness of neural decoding algorithms. This is particularly important in low-quality recording conditions, where maintaining the quality of neural data are essential for iBMI.

B. Behavior training paradigm

The methods used are as described previously.[80,81] Briefly, rats were trained on a skilled reach task for up to 1 week before surgery. Prior to training on the lever press behavior, the rats underwent at least 8 hours of water deprivation that could motivate them to complete the lever-pressing task. All training took place in a rectangular behavioral box (30 cm long, 60 cm high, 30 cm deep) with a water supply positioned in the corner. A lever was set diagonally to the water supply at a height of 15 cm, corresponding to the height of a rat standing bipedally. One side of the lever was adjacent to the wall of the behavior box, while the other side featured a transparent acrylic plate with a 6 cm wide slit, as illustrated in Fig. 6.

For the rat to press the lever and receive the water reward, it had to position its body close to the wall, facing the lever, allowing its right forelimb to reach into the 6 cm wide slit to press the lever. This setup also facilitated the color Charge Coupled Device (CCD) camera (DFK 21BF04, Imaging Source, Bremen, Germany) with a standard lens (25 cm focal length) in capturing consistent forelimb movement trajectories. The configuration allowed for the effective use of two-dimensional spatial coordinates (x and y axes) to characterize the trajectory information while maintaining a constant in-focus depth along the z-axis. The CCD camera was positioned approximately 25 cm away from the acrylic plate.

The water-restricted animals were trained to press the lever with their right forelimb to trigger a water pump for a reward without any cues. Each successful lever press delivered 0.25 ml of water. Training sessions lasted 1 h per day until the rats could consistently perform the water-reward lever-pressing task at least five times. Once the rats mastered this task, they underwent surgery for neural implantation.

C. Surgical procedures

Once the rats met the criterion of continuously performing the forelimb reaching to lever-press for a water reward at least five times within 1 h per day over three consecutive training days,[80,81] we implanted chronic microwire electrode arrays into the M1 of the left hemisphere of animal brains. Rats were anesthetized with a combination of 40 mg/kg Zoletil 50® (Vibac Laboratories, Carros, France) and 0.008 mg/kg Domitor® (Pfizer, Karlsruhe, Germany) via intramuscular injections. Each rat was positioned on a stereotaxic apparatus (model 51500, Stoelting Co., Kiel, WI, USA), and the scalp was incised to expose the bregma and lambda suture landmarks. Subsequently, an eight-channel Teflon-coated tungsten microelectrode array (item # 100211, internal diameter of 50 μm, California Fine Wire Co., Grover Beach, CA, USA) was implanted into the layer V of M1 of the left hemisphere of the rat brain (1.0–2.0 mm anterior, 1.9–2.7 mm left-lateral to bregma, and 1.5 mm ventral to the cortical surface). To confirm that the electrode implantation sites accurately correspond to the region controlling the contralateral forelimb, intracortical microstimulation (ICMS) was performed following the implantation of the electrode array. Rather than conducting a detailed mapping of all ICMS-induced neural responses,[82–84] our approach focused on identifying cortical sites where stimulation elicited distinct contralateral forelimb movements (e.g., wrist extension and forelimb supination). These motor responses served as a functional indicator for refining electrode positioning, ensuring the array was placed in the M1 regions crucial for decoding forelimb movements. In this study, the implantation coordinates were initially determined based on well-established motor representation maps from prior studies.[81,85–88] The ICMS involved using an isolated pulse stimulator (model 2100, A-M Systems Inc., Sequim, WA, USA) that delivered a 40 ms train of 0.2 ms square-wave monophasic cathodal pulses at a frequency of 350 Hz to the microelectrodes (impedance: 200–400 kΩ at 1 kHz). The intensity of the stimulation current is determined based on previous research.[86] A supplementary ground wire was securely wound around a stainless-steel screw (Shoukin Industry Co., Ltd., New Taipei City, Taiwan), which was inserted into the skull 3 mm posterior to the lambda point and connected to the cerebellum. During surgery of neural implantation, ICMS-induced motor responses (https://zenodo.org/records/15037196) were used to fine-tune electrode placement while maintaining controlled surgical durations to uphold ethical and experimental standards. Following implantation, dental cement (type 1 class 1, Hygenic Corp., Akron, OH, USA) was applied to affix the microelectrode array to the skull. The rat was removed from the stereotaxic frame and placed within the homeothermic blanket, upon which the animal was monitored for anesthetic recovery. Each rat was moved to a recovery area until the rat was able to maintain an upright posture and locomote freely. Once stabilized, the rat was returned to its home cage. Following implant surgery, rats were allowed one week of recovery, after which electrophysiological recordings of the left hemisphere and movement trajectory capture of the contralateral reaching forelimb (right) were simultaneously conducted under the corresponding lever-pressing task for a water reward.

D. Electrophysiological and behavioral data acquisition

After the recovery period, a multichannel neural data acquisition system (MAP, Plexon Inc., Dallas, TX, USA) integrated with a video-tracking system (CinePlex, Plexon Inc., Dallas, TX, USA) was used for neurophysiological recordings while the rats performed the reaching task in the behavior box, as shown in Fig. 6. Electrophysiological signals were routed through a unit-gain headstage and a preamplifier, followed by two separate analog filters: one for low-frequency LFP signals (0.7–300 Hz) and one for high-frequency neuronal MUAs (100–8 kHz). MUA signals underwent further filtering with an effective low-cut frequency of 300 Hz by the MAP. The sampling rate used for all recordings was 30 kHz. For the forelimb movement trajectory recording, a blue ring marker on the right forelimb of the rats was tracked using a video-tracking system equipped with a charge-coupled device (CCD) camera (DFK21F04, Imaging Source, Bremen, Germany) with a 30 Hz sampling rate in 640 × 480 RGB format. Both videos and neural recording data were combined within the same file, facilitating the synchronization of forelimb movement trajectory with neural recordings. Therefore, the recorded LFPs and MUAs on each channel for each electrode site, as well as timestamps generated by a transistor–transistor logic (TTL) pulse for the lever-pressing event were time-stamped and recorded simultaneously by the MAP system.

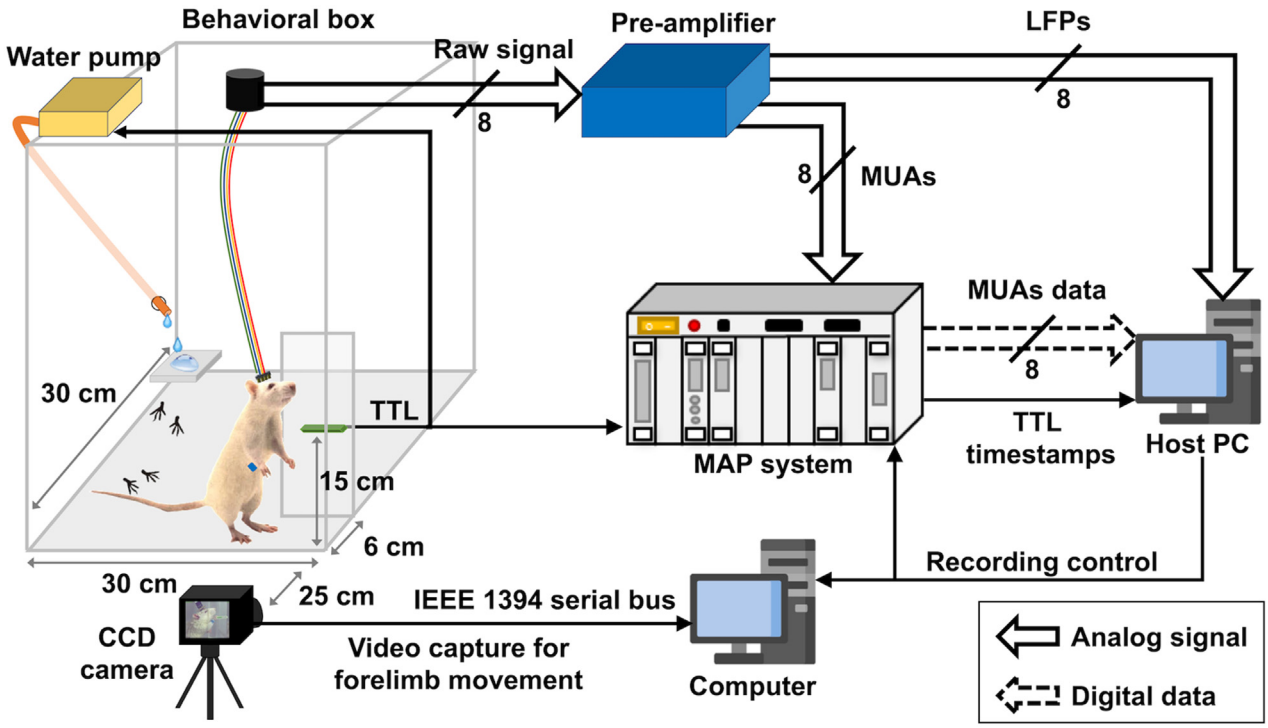

FIG. 6. Experimental setup for simultaneous recording of neural signals and video tracking of forelimb movement during a water-reward forelimb-reaching task. A rat implanted with a microelectrode array was placed in a transparent behavioral box ($30 \times 30\ cm^2$, 60 cm in height). During the execution of the water-reward forelimb-reaching task, a Host PC simultaneously controlled both the MAP system for neural signal recording and a separate computer for behavioral video recording. A CCD camera was positioned 25 cm away from the behavioral box to capture the rat's right forelimb movements during the task. When the rat pressed the lever, a TTL (Transistor-Transistor Logic) signal was generated to trigger the water pump, delivering a water reward, and was simultaneously recorded by the MAP system. The raw signals from eight recording channels of the microelectrode array, collected through the headstage fixed on the rat's head, were transmitted to a pre-amplifier, which separated the signals into MUAs and LFPs with high pass and low pass filters, respectively. The MUAs and LFPs were then digitized data by the MAP system using one National Instruments A/D (NIDAQ, PCI-6070E) board in the host computer. The Host PC recorded the MUA data, LFPs, and TTL timestamps simultaneously, facilitating precise synchronization of neural and behavioral data.

E. Data analysis and determination of MUA and LFP neural features

The rat's forelimb-reaching lever-pressing movement was tracked using a CCD camera with a sagittal view with a 90×90 mm window. The initial forelimb position during reach movement, set at coordinates $x = 0$ and $y = 0$, was defined as when the blue-coded alert wristband worn on its right forelimb first appeared in the view window at video frame #0. Sequentially, it took the rat approximately 363 ms (11 frames) to complete reaching and pressing the lever with its forelimb while standing bipedally completely as shown in Fig. 7(a). Neural features, derived from sequences of binned MUA counts and binned LFP power, were utilized to interpret forelimb reach movements. These neural features were segmented into 10-time bins per experimental trial, based on a TTL event triggered by lever pressing, as depicted in Fig. 7(b). Specifically, neural features were lagged 3 time bins before TTL event to represent the time delay between neural features and the forelimb movement. Each trial with a length of 10 time bins included 8 time bins before and 2 time bins after the 3rd time-bin lag prior to lever pressing.[81,85] This was because we observed that the rat took an additional 2-time bins to press the lever to the bottom and complete the lever-pressing task.

During a forelimb-reaching trial, significant increases in MUA firing counts were observed [Fig. 7(b), upper panel]. Additionally, the analysis of the binned time–frequency spectrum revealed increasing normalized LFP powers (Z score) in both low frequencies (0.7–30 Hz) and higher frequencies (30–300 Hz), particularly in the LFP power corresponding to the β, γ, and γ' bands [Fig. 7(b), middle and bottom panels]. Therefore, combining high-frequency MUA data with the lower-frequency LFP data allowed for a more comprehensive representation of the underlying neural mechanisms, leading to more accurate predictions of forelimb movement. In this study, MUA counts were extracted by high-pass filtering the raw neural signals (above 300 Hz). Subsequent processing converted the raw MUA spike train per channel (electrode) into sequences of binned spike counts with a bin width of 33 ms. The corresponding processing steps were as follows: spikes were detected by comparing the high-pass filtered signal to a voltage threshold, which was determined as three times the standard deviation of the baseline noise[81] across the entire 27-day recording period. Once the spikes were detected, their precise times of occurrence were noted. These MUA timestamps were then segmented into 33-ms bins, matching the recording frame duration of the video-tracking system (30 FPS). For each recording channel c (where $c = 1, 2, \ldots, 8$), the number of detected MUA spikes within each time bin was counted. Let f_b^c

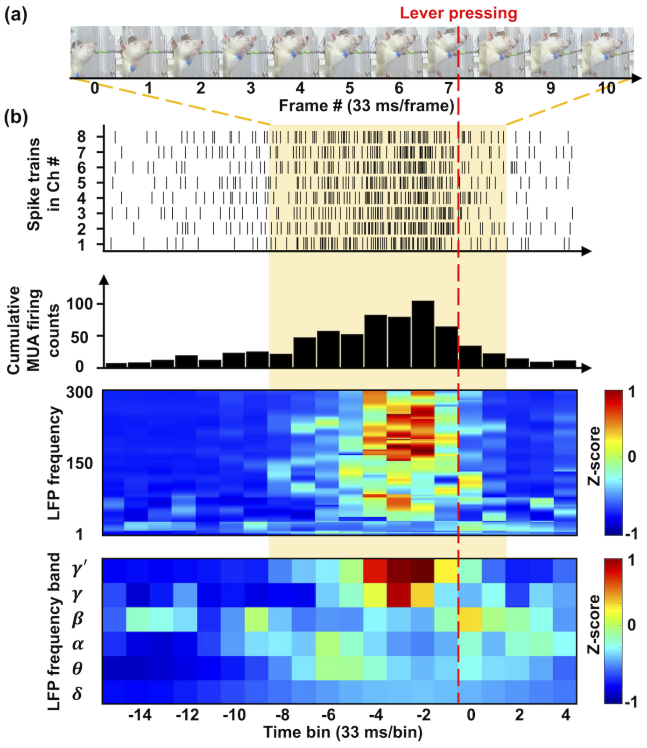

FIG. 7. Simultaneous video tracking and neural features during a forelimb-reaching task. (a) Representative frames from video tracking of a rat completing a forelimb-reaching trial, showing movement from frame #0 to frame #10, with a frame interval of 33 ms. The red dashed line indicates the moment of lever pressing, which occurs at frame #7. The video shows 8 frames before and 3 frames after the lever-pressing event, highlighting the critical phases of the forelimb-reaching movement. (b) The orange-shaded region represents the neural activity during the forelimb-reaching movement, covering the time bin from −10 to 0. The top plot shows the spike trains recorded from eight channels, indicating a noticeable increase in spike activity as the rat approaches the lever-pressing moment. The middle plot displays cumulative MUA counts, which are significantly elevated during this period, particularly near the lever-pressing event. The bottom two plots show changes in LFP power across various frequency bands (δ, θ, α, β, γ, and γ'), where increased LFP power is observed from −10 to 0 time bins compared to other time periods. The neural features, including spike trains, MUA counts, and LFP power, exhibit greater changes during the forelimb-reaching phase, indicating heightened neural activity associated with the motor task.

denotes the number of determined MUA counts in the b^{th} time bin of the c^{th} channel. This produces a sequence of binned MUA firing counts F^c over time for each recording channel, denoted by

$$F^c = \begin{bmatrix} f_1^c & \cdots & f_b^c \end{bmatrix}, \quad \text{for} \quad b = 1, 2, \ldots, 10. \tag{1}$$

Thus, sequences of binned MUA firing counts with a bin length of ten from eight recording channels, represented as $\boldsymbol{F}^{8\times10}$, are used as input features for the neural decoder during a forelimb-reaching trial.

Frequency-spectrum features were widely used for processing LFPs; therefore, LFP raw data were further down-sampled to a 1-kHz sampling rate and converted to power spectral density using a short-time Fourier transform with a Hanning window of $\frac{1}{f_m}$ ms in length[89,90] and time step of 33-ms, where f_m is the minimum frequency of each LFP frequency bands (using the spectrogram function from the Signal Processing Toolbox, MATLAB R2019a, MathWorks). The segmentation of frequency bands and corresponding window sizes are as follows: δ [1–3 Hz]: 1000 ms, θ [4–8 Hz]: 250 ms, α [9–12 Hz]: 111 ms, β [13–30 Hz]: 77 ms, γ [31–80 Hz]: 66 ms, and γ' [81–300 Hz]: 66 ms. To ensure stable frequency resolution and proper spectral separation, the window size for the γ and γ' bands is fixed at 66 ms, considering that our time step is fixed at 33 ms. The corresponding spectrogram of each frequency band was then normalized to the Z-score using the mean and standard deviation (SD) across a baseline period [−20, −15 time bin] of each trial, in the respective frequency ranges, to get the Z values in power for each LFP band with respect to time bin. Therefore, the sequence of binned LFP power for each recording channel was denoted by

$$P^c = \begin{bmatrix} p^c_{\delta,1} & & p^c_{\delta,b} \\ p^c_{\theta,1} & & p^c_{\theta,b} \\ p^c_{\alpha,1} & \cdots & p^c_{\alpha,b} \\ p^c_{\beta,1} & & p^c_{\beta,b} \\ p^c_{\gamma,1} & & p^c_{\gamma,b} \\ p^c_{\gamma',1} & & p^c_{\gamma',b} \end{bmatrix}, \quad \text{for} \quad b = 1, 2, \ldots, 10, \tag{2}$$

where $p^c_{\delta,b}$, $p^c_{\theta,b}$, $p^c_{\alpha,b}$, $p^c_{\beta,b}$, $p^c_{\gamma,b}$, and $p^c_{\gamma',b}$ represented the per-bin LFP power for each frequency band in the b^{th} bin of the c^{th} channel. Thus, sequences of binned LFP power across six frequency bands with a bin length of ten, from eight recording channels, represented as $\boldsymbol{P}^{48\times10}$, are used as input features for the neural decoder during a forelimb-reaching trial.

F. Confidence-weighted Bayesian linear regression (CW-BLR) for imputation of neural features

The CW-BLR model was developed to impute binned MUA spike counts and LFP power across six frequency bands when signal degradation was observed between the 8th and 27th recording days. The CW-BLR workflow, illustrated in Fig. 8, evaluates neural data quality using metrics, such as MUA *SNR*[11] and LFP *Coh*[12] (also see Sec. V F 1 for definitions). These metrics are benchmarked during the baseline period (recording days 1–7; see supplementary Note 1) to establish reference values. Data collected from days 8–27 are assessed against these benchmarks to determine their usability. When MUA *SNR* or LFP *Coh* remains within one SD of the baseline mean, the neural data are directly utilized for movement decoding. However, if either metric falls more than one SD below the baseline mean, the data are flagged as low-quality, and confidence weights, derived from the quality metrics, are introduced to adjust their influence on the model (Sec. V F 1). These confidence weights reduce the impact of degraded signals during subsequent regression steps, preserving the robustness of the CW-BLR framework.

For low-quality data, the Bayesian linear regression framework performs imputation of MUA spike counts and LFP power across six frequency bands, incorporating temporal, spatial, and cross-modality dependencies based on baseline recordings (Sec. V F 2). Regression coefficients estimated from high-quality recordings (Sec. V F 1) are applied to degraded signals while accounting for uncertainty through the influence of reduced confidence weights. This approach ensures

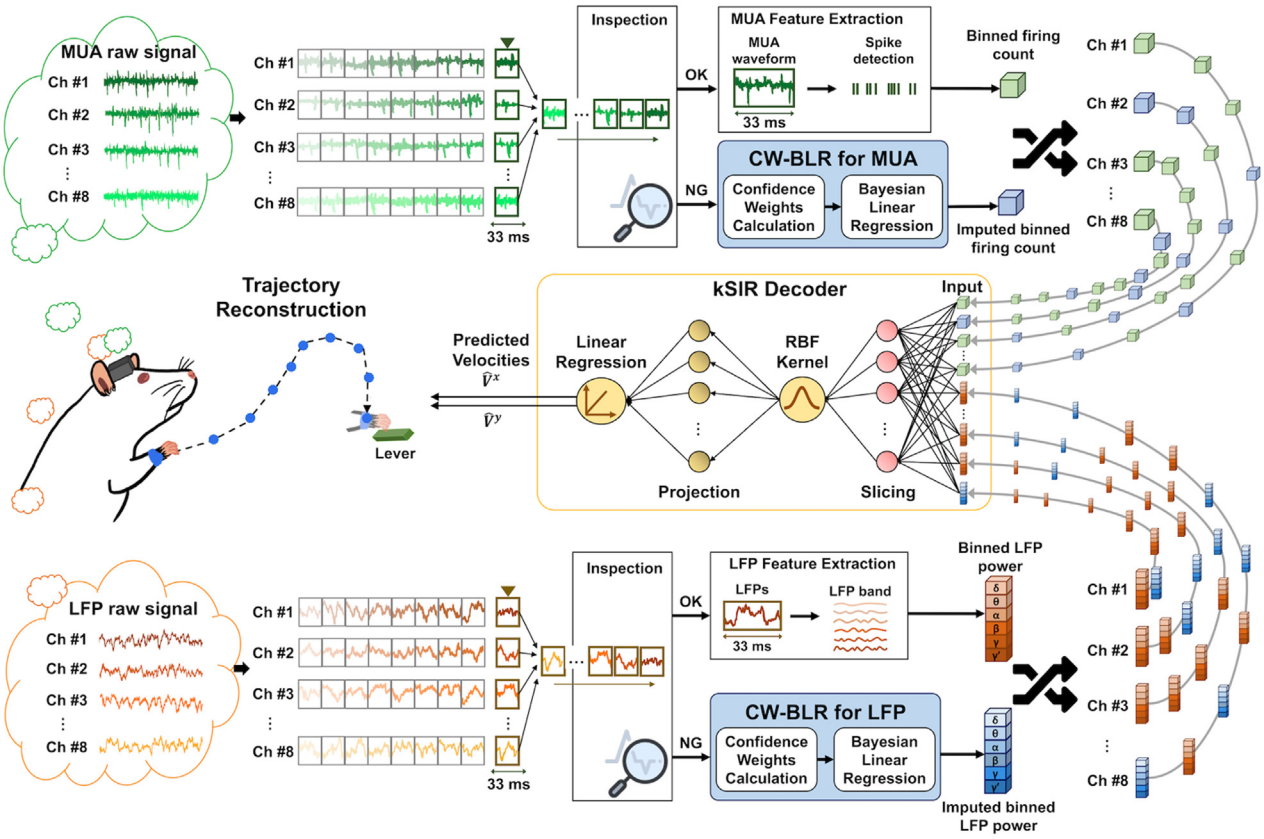

FIG. 8. Framework for neural imputation and forelimb trajectory prediction. Forelimb movement-associated MUA (green) and LFP (orange) signals are segmented into 33 ms intervals (bin length) and inspected individually. Each segment is labeled "OK" or "NG" based on criteria outlined in Tables S1 and S2 of supplementary Note 1. Signals labeled "OK" undergo feature extraction, converting them into neural features of MUA firing counts or LFP power across six frequency bands. "NG" signals are processed through CW-BLR to impute corresponding missing or degraded neural features, shown as blue boxes. These binned features are fed into the kSIR decoder, which predicts velocities $\hat{V}^x$ and $\hat{V}^y$ to reconstruct the forelimb trajectory. Further details on the kSIR decoder are available in supplementary Note 2.

the stability of regression coefficients even in the presence of signal degradation. Following imputation (Sec. V F 4), the reconstructed neural features are passed to the kernel-sliced inverse regression (kSIR) decoder. This final step ensures reliable signal reconstruction and robust forelimb movement decoding, maintaining decoding performance despite the presence of low-quality neural signals.

1. Confidence weights calculation based on MUA SNR and LFP Coh

To handle the quality of raw MUA and LFP signals, confidence weights were introduced based on MUA *SNR* and LFP spectral *Coh*. These weights were then computed for each time bin and channel, reflecting the corresponding signal quality of both modalities and down-weighting low-quality neural recordings. *SNR* for raw MUA data were calculated as the ratio of MUA signal power to background noise power as follows:

$$SNR_{MUA}(b,\,c) = 20 \cdot \log_{10} \frac{\frac{1}{N}\sum_{n=1}^{N} RMS(MUA)^{b}}{\sigma_{noise}}, \tag{3}$$

where $RMS(MUA)^{b}$ denoted the root mean square of 33-ms-long raw MUA signal in the bth time bin, $b = 1, \ldots, 10$, and the cth channel, $c = 1, \ldots, 8$. The SD of background noise, σ_{noise}, was estimated from pure noise segments without any spikes.[11]

The MUA confidence weight $w_{MUA}(b,\,c)$ was then defined as

$$w_{MUA}(b,\,c) = \frac{SNR_{MUA}(b,\,c)}{SNR_{MUA}(b,\,c) + \alpha_{MUA}}, \tag{4}$$

where α_{MUA} is set to 3.5 to adjust the sensitivity of the weighting for mean MUA *SNR* from 1st to 7th recording day, thereby controlling the reduction in confidence for the degradation of MUA signals.

Bin-by-bin *Coh* analysis was used to assess the quality of the raw LFP signals across six frequency bands. This method evaluates how the spectral properties of the LFP signals from the 8th to the 27th day deviate from the baseline period from 1st to 7th recording day. For each frequency band $S \in \{\delta,\,\theta,\,\alpha,\,\beta,\,\gamma,\,\gamma'\}$ and each time bin b of the cth channel, the *Coh* was calculated using a sliding 500-ms-long window with a 467-ms-long overlap.

The magnitude-squared coherence $Coh_b^c(S)$ for cth channel at bin b was computed between the baseline PSD averaged from 1st to

7th recording day and test PSD (8th to 27th day) within the same frequency band

$$Coh_b^c(S) = \frac{\left|\left\langle PSD_c^{baseline,test,b}(S)\right\rangle\right|^2}{\left\langle PSD_c^{baseline,b}(S)\right\rangle \cdot \left\langle PSD_c^{test,b}(S)\right\rangle}, \quad (5)$$

where $PSD_c^{baseline,b}(S)$ is the PSD in a given frequency band $S \in \{\delta, \theta, \alpha, \beta, \gamma, \gamma'\}$ of the cth channel at the bth time bin during the baseline period. $PSD_c^{test,b}(S)$ is the PSD in a given frequency band $S \in \{\delta, \theta, \alpha, \beta, \gamma, \gamma'\}$ of the cth channel at the bth time bin during the test period from the 8th to the 27th day.[91]

The LFP confidence weight $w_{LFP}^S(b, c)$ was defined as

$$w_{LFP}^S(b, c) = \frac{Coh_b^c(S)}{Coh_b^c(S) + \alpha_{LFP}^S}, \quad S \in \{\delta, \theta, \alpha, \beta, \gamma, \gamma'\}, \quad (6)$$

where $\alpha_{LFP}^{\delta} = \alpha_{LFP}^{\theta} = \alpha_{LFP}^{\alpha} = \alpha_{LFP}^{\beta} = 0.1$. The high *Coh*s were observed in the low- and mid-frequency LFP bands (δ, θ, α, and β) were found, prompting the assignment of lower values for α_{LFP}^{δ}, α_{LFP}^{θ}, α_{LFP}^{α}, and α_{LFP}^{β} to avoid overly penalizing moderately noisy signals within these frequency ranges. The higher LFP frequency bands, γ and γ', are particularly susceptible to attenuation by higher neural tissue-electrode impedance,[13] leading to lower *Coh*. As a result, the corresponding α_{LFP}^{γ} and $\alpha_{LFP}^{\gamma'}$ should be set to 1.

The final combined confidence weight for low-quality binned MUA counts and LFP power (time bin b and channel c) was computed by multiplying the individual MUA and LFP confidence weights as follows:

$$w(b, c) = w_{MUA}(b, c) \times w_{LFP}^{\delta}(b, c) \times w_{LFP}^{\theta}(b, c) \times w_{LFP}^{\alpha}(b, c) \times w_{LFP}^{\alpha}(b, c) \times w_{LFP}^{\beta}(b, c) \times w_{LFP}^{\gamma}(b, c) \times w_{LFP}^{\gamma'}(b, c). \quad (7)$$

Therefore, this combined weight $w(b, c)$ was used to adjust the contribution of low-quality binned MUA counts and LFP power during imputation, lowering the influence of degradation of neural recordings over time.

2. Prior distribution of MUA and LFP in Bayesian linear regression

BLR was applied to impute binned MUA firing count and LFP power across six frequency bands. The model leveraged temporal, spatial, and cross-modality dependencies, with confidence weights reducing the influence of low-quality neural recordings. The method was applied to each time bin and recording channel.

The scalar response variable $\hat{f}_b^c$ for those missing or degraded bins, which was modeled using BLR

$$\hat{f}_b^c = \boldsymbol{X_c}(b)\beta_{MUA} + \epsilon_{MUA}, \quad (8)$$

where $\hat{f}_b^c \in \mathbb{R}$ is the binned MUA firing count at the bth time bin of the cth channel. $\boldsymbol{X_c}(b) \in \mathbb{R}^{1\times 35}$ is the feature vector in CW-BLR model, which is determined using the high-quality neural recording data collected during the baseline period, specifically from the 1st to the 7th recording day. The prior distribution regression coefficients $\beta_{MUA} \in \mathbb{R}^{35}$ for MUA firing count contain one coefficient for each feature in the feature vector $\boldsymbol{X_c}(b)$. $\epsilon_{MUA} \sim \mathcal{N}(0, \sigma_{MUA}^2)$ is the Gaussian noise term.

Similarly, the scalar response variable $\hat{p}_b^c$ for those missing or degraded bins, which was modeled as

$$\hat{p}_b^c = \boldsymbol{X_c}(b)\beta_{LFP}(S) + \epsilon_{LFP}(S), \quad (9)$$

where $\hat{p}_b^c \in \mathbb{R}$ is the scalar response variable representing the binned LFP power for the corresponding time bin and channel in a given frequency band $S \in \{\delta, \theta, \alpha, \beta, \gamma, \gamma'\}$. $\boldsymbol{X_c}(b) \in \mathbb{R}^{1\times 35}$ is the actual feature vector. $\beta_{LFP}(S) \in \mathbb{R}^{35\times 1}$ is the regression coefficients for prior distribution in frequency band S. $\epsilon_{LFP}(S) \sim \mathcal{N}(0, \sigma_{LFP(S)}^2)$ is the Gaussian noise term.

The actual feature vector $\boldsymbol{X_c}(b)$ at time bin b and channel c was designed to incorporate temporal, spatial, and cross-modality dependencies. Each feature vector consists of 35 elements, representing MUA firing count and LFP power from neighboring time bins and channels. The dimension of the actual feature vector is labeled as $\boldsymbol{X_c}(b) \in \mathbb{R}^{1\times 35}$. Here, the feature vector $\boldsymbol{X_c}(b)$ is represented as

$$\boldsymbol{X_c}(b) = \begin{bmatrix} f_b^c & f_{b-1}^c & f_{b+1}^c & f_b^{c-1} & f_b^{c+1} & p_{S,b}^c & p_{S,b-1}^c & p_{S,b+1}^c & p_{S,b}^{c-1} & p_{S,b}^{c+1} \end{bmatrix}, S \in \{\delta, \theta, \alpha, \beta, \gamma, \gamma'\}, \quad (10)$$

where actual MUA features are extracted from the dataset during the 1st to 7th recording day. m_b^c, the firing count at the current time bin and channel; f_{b-1}^c and f_{b+1}^c, the counts from the previous and next time bins; and f_b^{c-1} and f_b^{c+1} the counts from the previous and next channels. These contribute 5 elements to the feature vector. For the six LFP frequency bands, the actual LFP features from the dataset during the 1st to 7th recording day include: $p_{S,b}^c$, the power at the current time bin and channel; $p_{S,b-1}^c$ and $p_{S,b+1}^c$, the power at the previous and next time bins; and $p_{S,b}^{c-1}$ and $p_{S,b}^{c+1}$, the power at the previous and next channels. Each band contributes five features, resulting in a total of 30 LFP features. *Note: Mirror padding (reflection) is applied to handle boundary conditions when the channel number is at the edges (1 or 8) or when the time bin is at the boundaries (1 or 10). This method creates symmetric "virtual" neighbors by reflecting the values at the boundary. Specifically, when* $c = 1$, $f_b^{c-1} = f_b^c$ *and* $p_{S,b}^{c-1} = p_{S,b}^c$; *when* $b = 1$, $f_{b-1}^c = f_b^c$ *and* $p_{S,b-1}^c = p_{S,b}^c$; *when* $c = 10$, $f_b^{c+1} = f_b^c$ *and* $p_{S,b}^{c+1} = p_{S,b}^c$; *when* $b = 10$, $f_{b+1}^c = f_b^c$ *and* $p_{S,b+1}^c = p_{S,b}^c$.

The prior distribution regression coefficients β_{MUA} and $\beta_{LFP}(S)$ are determined by fitting a BLR model to the high-quality data from the 1st to 7th recording days. During this process, the hyperparameters α_{MUA} and α_{LFP} are effectively set to zero or not used, as no down-weighting is necessary for this high-quality data. The MUA *SNR* and

LFP spectral *Coh* are within acceptable ranges during the period of 1st to 7th recording days, meaning the data are reliable and does not require any sensitivity adjustments. Therefore, all data points contribute equally to the estimation of the prior distribution regression coefficients, allowing for a straightforward calculation of β_{MUA} and $\beta_{LFP}(S)$ from the feature vectors constructed from neighboring time bins and channels.

3. Posterior distribution of regression coefficients

The individual regression model uses the high-quality data with $\mathfrak{N}$ trials from the 1st to 7th recording days per animal to estimate the posterior distribution of regression coefficients, which are then applied to the degraded data for imputation.

a. Posterior distribution for MUA regression coefficients. For MUA firing count, the posterior distribution of the regression coefficients β_{MUA} is Gaussian with a posterior mean $\mu_{\beta_{MUA}}$ and a covariance matrix $\sum_{\beta_{MUA}}$. The posterior is derived as follows:

The regression coefficients for prior distribution β_{MUA} is typically modeled as a multivariate Gaussian distribution

$$?(\beta_{MUA}) = \frac{1}{(2\pi)^{\frac{35}{2}}\left|\sum_0^{MUA}\right|^{\frac{1}{2}}} \times \exp\left(-\frac{1}{2}\left(\beta_{MUA}-\mu_0^{MUA}\right)^T\left(\sum_0^{MUA}\right)^{-1}\left(\beta_{MUA}-\mu_0^{MUA}\right)\right), \tag{11}$$

where $\not{\mu}(\beta_{MUA})$ represents the probability density function (prior distribution) for the MUA regression coefficients β_{MUA}. $\mu_0^{MUA} \in \mathbb{R}^{35}$ is the prior mean vector for the coefficient, which contains the initial expected values of the MUA regression coefficients β_{MUA}. $\sum_0^{MUA} \in \mathbb{R}^{35\times35}$ is the prior covariance matrix, which represents the uncertainty (variance) in the prior knowledge about $\not{\mu}(\beta_{MUA})$. $\left|\sum_0^{MUA}\right|$ is the determinant of the covariance matrix $\sum_0^{MUA}$. $(\sum_0^{MUA})^{-1}$ is the inverse of the covariance matrix.

The likelihood for the MUA firing count, weighted by the confidence $w(b,\ c)$, is

$$L\left(f_b^c|\beta_{MUA}, \boldsymbol{X_c}(b)\right) = \frac{1}{\sqrt{2\pi\frac{\sigma_{MUA}^2}{w(b,c)}}}\exp\left(-\frac{\left(f_b^c-\boldsymbol{X_c}(\boldsymbol{b})^T\beta_{MUA}\right)^2}{2\frac{\sigma_{MUA}^2}{w(b,c)}}\right), \tag{12}$$

where f_b^c is the observed response variable of MUA firing count at time bin b and channel c. $\boldsymbol{X_c}(b)$ is the actual feature vector. β_{MUA} is the regression coefficient vector. σ_{MUA}^2 is the variance of the Gaussian noise term for the MUA data. $w(b,\ c)$ is the combined confidence weight for the low-quality binned MUA counts and LFP power, calculated from both MUA *SNR* and LFP *Coh* at six frequency bands.

After setting up the likelihood and the prior, the posterior distribution of the regression coefficients β_{MUA} is computed using Bayes' Theorem. The posterior captures the uncertainty in the estimated coefficients based on the observed data quality

$$\sum\nolimits_{\beta_{MUA}} = \left(\frac{1}{\sigma_{MUA}^2}X^T\boldsymbol{W}X + \sum\nolimits_0^{MUA} - 1\right)^{-1}, \tag{13}$$

$$\mu_{\beta_{MUA}} = \sum\nolimits_{\beta_{MUA}}\left(\frac{1}{\sigma_{MUA}^2}X^T\boldsymbol{W}F + \sum\nolimits_0^{MUA} - 1\mu_0^{MUA}\right), \tag{14}$$

where X^T is the transpose of the design matrix $X \in \mathbb{R}^{(8\times10\times\mathfrak{N})\times35}$. X is created by stacking feature vectors $\boldsymbol{X_c}(b)$ across all time bins and channels. $\boldsymbol{W} \in \mathbb{R}^{(8\times10\times\mathfrak{N})\times(8\times10\times\mathfrak{N})}$ is the diagonal matrix of confidence weights $w(b,\ c)$. $\sum_0^{MUA} - 1$ is the inverse of the prior covariance matrix. $F \in \mathbb{R}^{8\times10\times\mathfrak{N}}$ is the matrix of observed response variable of MUA firing count (f_b^c) across all time bins and channels and it is derived from the dataset collected during the first week with good quality recordings (1st to 7th recording day). The product $\sum_0^{MUA} - 1\mu_0^{MUA} \in \mathbb{R}^{35}$ for 35 features is used in the calculation of the posterior mean of the MUA regression coefficients in BLR model.

b. Posterior distribution for LFP regression coefficients. For LFP power, the posterior distribution of the regression coefficients $\beta_{LFP}(S)$ for each frequency band S is similarly Gaussian with a posterior mean $\mu_{\beta_{LFP}(S)}$ and a covariance matrix $\sum_{\beta_{LFP(S)}}$.

Assume a Gaussian prior for LFP regression coefficients $\beta_{LFP}(S)$:

$$\not{\mu}(\beta_{LFP}(S)) = \frac{1}{(2\pi)^{\frac{35}{2}}\left|\sum_0^{LFP(S)}\right|^{\frac{1}{2}}} \times \exp\left(-\frac{1}{2}\left(\beta_{LFP}(S)-\mu_0^{LFP(S)}\right)^T\left(\sum_0^{LFP(S)}\right)^{-1} \times \left(\beta_{LFP}(S)-\mu_0^{LFP(S)}\right)\right), \tag{15}$$

where $\mu_0^{LFP(S)}$ is the prior mean vector representing the prior expected values of the coefficients $\beta_{LFP}(S)$ for the LFP feature data. $\sum_0^{LFP(S)} \in \mathbb{R}^{35\times35}$ is the prior covariance matrix, representing the uncertainty (variance and covariance) between coefficients $\beta_{LFP}(S)$ for LFP feature data. $\left|\sum_0^{LFP(S)}\right|$ is the determinant of the covariance matrix $\sum_0^{LFP(S)}$. $(\sum_0^{LFP(S)})^{-1}$ is the inverse of the covariance matrix.

The likelihood function for binned LFP power is weighted by the confidence $w(b,\ c)$ of the observation and is defined as

$$L\left(p_{S,b}^c|\beta_{LFP}(S),\ \boldsymbol{X_c}(b)\right) = \frac{1}{\sqrt{2\pi\frac{\sigma_{LFP(S)}^2}{w(b,\ c)}}}\exp\left(-\frac{\left(p_{S,b}^c - \boldsymbol{X_c}(b)^T\beta_{LFP}(S)\right)^2}{2\frac{\sigma_{LFP(S)}^2}{w(b,\ c)}}\right), \tag{16}$$

where $p_{S,b}^c$ is the observed response variable of LFP power in frequency band S at time bin b and channel c. $\boldsymbol{X_c}(b)$ is the actual feature vector. $\beta_{LFP}(S)$ is the regression coefficient vector for the given frequency band S. σ_{LFP}^2 is the variance of the Gaussian noise term for the LFP data. $w(,\ c)$ is the combined confidence weight for low-quality binned MUA counts and LFP power, calculated from both MUA *SNR* and LFP *Coh* at six frequency bands.

The posterior distribution of $\beta_{LFP}(S)$ is given by

$$\sum_{\beta_{LFP}(S)} = \left(\frac{1}{\sigma^2_{LFP(S)}} X^T \boldsymbol{W} X + \sum_0^{LFP(S)} -1\right)^{-1}, \quad (17)$$

$$\mu_{\beta_{LFP}(S)} = \sum_{\beta_{LFP}(S)} \left(\frac{1}{\sigma^2_{LFP(S)}} X^T \boldsymbol{W} P_S + \sum_0^{LFP(S)} -1\mu_0^{LFP(S)}\right), \quad (18)$$

where $P_S \in \mathbb{R}^{8\times 10\times \mathfrak{N}}$ is the matrix of observed LFP power values for frequency band S across all time bins and channels. It is derived from the dataset recorded during the first week (1st to 7th recording day) when the signal quality is high. Other terms are similar to the definitions of the MUA posterior.

4. Imputation of MUA and LFP data

Imputation of MUA and LFP data are carried out from the 8th to the 27th recording days, specifically targeting periods when signal quality degrades. The decision to impute is based on the quality metrics of MUA *SNR* and LFP *Coh*, respectively, which were established during the baseline period (1st to 7th recording days). Imputation is triggered when the MUA *SNR* or LFP *Coh* of a specific channel and time bin during the 8th to the 27th recording days falls below the mean MUA *SNR* and mean LFP *Coh* recorded during the 1st to 7th days, exceeding one SD. When either the MUA *SNR* or the LFP *Coh* falls below their respective thresholds as shown in Tables S1 and S2 (see the quality criteria of neural recordings in the in supplementary Note 1), imputation is performed for that specific channel and time bin using the CW-BLR model. The imputation is executed using the posterior means of the regression coefficients as follows:

For imputed MUA firing counts

$$\hat{f}_b^c = \boldsymbol{X_c}(b)\mu_{\beta_{MUA}}. \quad (19)$$

For imputed LFP power in frequency S at time bin b and channel c

$$\hat{p}_{s,b}^c = \boldsymbol{X_c}(b)\mu_{\beta_{LFP}(S)}. \quad (20)$$

To evaluate the robustness of CW-BLR imputation on neural signals with degraded recording quality (from recording days 8 to 27), we compared the decoding performance of CW-BLR-imputed neural features with that of the actual (non-imputed) neural features for predicting forelimb trajectories using the kSIR decoder (see supplementary Note 2 for detailed algorithm implementation). Additionally, to thoroughly assess the effectiveness of CW-BLR in handling degraded neural signals, we compared its performance against other imputation algorithms, such as Mean-imp and GMM-EM, as described in supplementary Note 3. These comparisons specifically address the challenges associated with recording quality degradation observed from the 8th to the 27th recording day.

TABLE II. Experimental datasets. Neural data from forelimb-reaching trials recorded from the 1st to the 7th day were split into training and test sets at a 7:3 ratio for each animal. To assess changes in decoding performance over time, low-quality recordings were imputed, and the resulting sets were used to evaluate decoding performance for each animal from the 8th to the 27th recording day.

	1st–7th recording day		8th–27th recording day
Dataset Animal ID	Total number of training trial	Total number of testing trial	Number of testing trial per day (mean ± SD)
Rat #4	291	73	49.25 ± 5.77
Rat #6	269	67	52.48 ± 6.15
Rat #9	196	49	33.53 ± 4.63
Rat #10	375	94	61.34 ± 6.48

G. Neural decoder

Neural data were recorded from multiple forelimb-reaching trials across the 1st to the 27th recording day for each animal. Stable and high-quality recordings were obtained only during the 1st to 7th recording day, where each trial consistently captured forelimb-reaching movements along with well-defined neural activity in both MUA and LFP signals, as illustrated in Figs. S1 and S2 of supplementary Note 1. Therefore, only the dataset from these stable recording days was used and subsequently divided into training and testing sets at a 7:3 ratio to facilitate the development and evaluation of the kSIR neural decoder. A detailed description of the kSIR decoder implementation can be found in supplementary Note 2. To evaluate the decoder's performance, the root mean square error (RMSE) was used to measure the differences between the predicted and actual forelimb movement velocities along the x- and y-axes during forelimb-reaching movements. Data characteristics for four animals are summarized in Table II.

1. Optimization of the tuning parameters of kSIR decoder

This study chose the radial basis function (RBF) kernel for the kSIR decoder because of its capability to effectively capture nonlinear relationships in neural features.[92,93] Optimizing the kernel width parameter (σ) and regularization parameters (r) of the kSIR decoder with RBF kernel, specifically Gaussian distribution width in the RBF kernel and the sufficient dimension reduction of kSIR decoder, respectively, is essential for building a kSIR decoder that is accurate, efficient, and robust in prediction of forelimb movement. When σ is too small, the model overemphasizes local details, making it highly sensitive to noise and impairing its ability to learn the overall data distribution effectively. Conversely, when σ is too large, the model becomes overly smooth, losing critical distinctions between data clusters and reducing its ability to capture meaningful variations in neural activity. Empirical results have shown that $\sigma = 1$ provides an effective balance between local and global information, enhancing class separability while preventing overfitting.[92]

To refine this selection further, we conducted a more granular search around $\sigma = 1$, using six levels: $\sigma = 0.60$, 0.70, 0.80, 0.90, 1.00, and 1.10. For the r value, it is essential that $r > 0$ to prevent overfitting while maintaining the model's generalizability. Our optimization analysis identified the range $r = 0.08$, 0.09, 0.10, 0.11, 0.12, and 0.13 as the most effective, providing a stable balance between model flexibility and robustness. Testing larger ranges outside this interval resulted in either excessive regularization (leading to underfitting) or insufficient regularization (increasing model variance).

To ensure rigorous parameter selection, we applied fivefold cross-validation, systematically evaluating performance across all parameter

combinations in the kSIR model. The kSIR model was trained for each animal's training set during the 1st to 7th recording day, as shown in Table II. This process was used to determine the optimal σ and r pair that resulted in the best decoding performance for predicting forelimb movement velocity along the x-axis and y-axis, respectively, with the lowest RMSEs.

2. Neural feature weight distribution of trained kSIR model vs neural representation of forelimb movement

Comparing the neural feature weight distribution of a trained kSIR model with the neural representation of forelimb movement offers valuable insight into how various neural features contribute to movement decoding. This comparison helps assess the decoding model's performance and biological plausibility, enhancing our understanding of how neural signals translate into behavior and how the model captures the relevant neural dynamics for predicting forelimb movements.

To assess the significance of input neural features, including binned MUA spike count and LFP power, for the kSIR model in predicting forelimb velocities along x and y axes, respectively, during a forelimb-reaching task, the percentage contributions (% *CONTRIB*)[94,95] were calculated. Specifically, this involved determining the % *CONTRIB* for the binned MUA neural feature per recording channel and the total LFP power across eight recording channels for each frequency band $S \in \{\delta, \theta, \alpha, \beta, \gamma, \gamma'\}$, respectively, using the following formula:

$$\%\, CONTRIB_c^{MUA} = \frac{\omega_c^{MUA}}{\sum_{c=1}^{8} \omega_c^{MUA} + W_\delta^{LFP} + W_\theta^{LFP} + W_\alpha^{LFP} + W_\beta^{LFP} + W_\gamma^{LFP} + W_{\gamma'}^{LFP}} \times 100\%, \tag{21}$$

$$\%\, CONTRIB_{S\in\{\delta,\theta,\alpha,\beta,\gamma,\gamma'\}}^{LFP} = \frac{W_S^{LFP}}{\sum_{c=1}^{8} \omega_c^{MUA} + W_\delta^{LFP} + W_\theta^{LFP} + W_\alpha^{LFP} + W_\beta^{LFP} + W_\gamma^{LFP} + W_{\gamma'}^{LFP}} \times 100\%, \tag{22}$$

where ω_c^{MUA} represents the weight associated with the cth input neural feature of binned MUA spike count in the kSIR decoder, for $c = 1, \ldots, 8$. W_S^{LFP} denotes the sum of weights for LFP power across eight recording channels for a given frequency $S \in \{\delta, \theta, \alpha, \beta, \gamma, \gamma'\}$. The sum of $\{\%\, CONTRIB_c^{MUA}\}_{c=1}^{8}$ and $\%\, CONTRIB_{S\in\{\delta,\theta,\alpha,\beta,\gamma,\gamma'\}}^{LFP}$ is 100%.

Additionally, MIC method[96,97] was employed to quantify the functional mapping between input neural features and the kinematic parameters of actual forelimb movement velocities along x and y axes, respectively, during a forelimb-reaching task. MIC was calculated for each forelimb-reaching trial in individual animals, and the correlation indices across all trials were used to evaluate the overall correlation. The MIC between a sequence of binned MUA counts and kinematic parameters MIC_{V,M^c} was computed as follows:

$$I_c(V; M^c) = H(V) + H(M^c) - H(V, M^c), \tag{23}$$

$$MIC_{V,M^c} = \max_{n_V \times n_{M^c} \le 10^{0.6}} \left(\frac{I_c(V; M^c)}{log2\left(min\left(n_V, n_{M^c}\right)\right)} \right), \tag{24}$$

where M^c denoted the sequence of binned MUA counts recorded from the cth channel. V denoted the actual velocity of forelimb movement from the 1st to the 10th time bin in a single axis (x-velocity or y-velocity). $H(\cdot)$ were the marginal entropies of the dataset and $H(\cdot, \cdot)$ were the joint Shannon entropies. $I_c(V; M^c)$ was the value of MIC_{V,M^c} across all possibilities of the dividing range $n_V \times n_{F_S^c} \le 10^{0.6}$. The maximum across all possible values of MIC_{V,M^c} was indicated as $\max_{n_V \times n_{M^c} \le 10^{0.6}}$. $I_c(V; M^c)$ was normalized by $log_2\left(min\left(n_V, n_{M^c}\right)\right)$ with V and M^c partitioned into $n_V \times n_{M^c}$ grid. To avoid trivial partitioning, n_V and n_{M^c} were considered when their product was less than the trial length of 10, i.e., $n_V \times n_{M^c} \le 10^{0.6}$.

The MIC of the sequence of binned LFP power in each frequency band and kinematic parameters was computed, respectively, as follows:

$$I_c\left(V; P_S^c\right) = H(V) + H\left(P_S^c\right) - H\left(V, P_S^c\right), \tag{25}$$

$$MIC_{V,P_S^c} = \max_{n_V \times n_{P_S^c} \le 10^{0.6}} \left(\frac{I_c(V; P_S^c)}{\log2\left(\min\left(n_V, n_{P_S^c}\right)\right)} \right), \tag{26}$$

where P_S^c denoted the sequence of binned LFP power for a given frequency band $S \in \{\delta, \theta, \alpha, \beta, \gamma, \gamma'\}$ in the cth channel. $I_c(V; P_S^c)$ was normalized by $\log_2\left(\min\left(n_V, n_{P_S^c}\right)\right)$ with V and P_S^c partitioned into $n_V - by - n_{P_S^c}$ grid and $n_V \times n_{F_S^c} \le 10^{0.6}$. MIC_{V,P_S^c} was obtained by computing the maximum over all possible value of $I_c(V; P_S^c)$. The magnitude of correlation was stronger with a higher MIC value, with values consistently ranging between 0 and 1.

H. Statistical analysis

Since our dataset was confirmed to deviate from normality, the nonparametric Friedman test followed by the Dunn–Bonferroni post hoc test was used to analyze differences in decoding performance (RMSE) between the actual and imputed neural features from the 8th to the 27th recording day. Given that our dataset involved two types of neural feature combinations ($N = 2$) and ten time bins ($T = 10$), the significance level was adjusted to to $p < 0.0025$ [adjusted p-value $= 0.05/(N \times T)$] to account for multiple comparisons.

The execution time of CW-BLR was compared to GMM-EM and Mean-imp by using the Kruskal–Wallis test ($p < 0.05$). To compare the decoding performance of the CW-BLR method with the Mean-imp and GMM-EM methods from the 8th to the 27th recording day, the nonparametric Friedman test followed by the Dunn–Bonferroni post hoc analysis was conducted at $p < 0.05$. Considering that this

dataset comprised three distinct imputation methods ($N = 3$) and ten time bins ($T = 10$), the significance level was adjusted to $p < 0.00167$ (adjusted p-value $= 0.05/(N \times T)$) to correct for multiple comparisons.

Additionally, to validate the long-term decoding robustness of the CW-BLR method for low-quality neural data, the Wilcoxon signed-rank test was applied at $p < 0.05$, comparing it against other imputation methods (Mean-imp and GMM-EM). All data are presented as mean ± SD. Statistical analyses were performed using SPSS version 26.0 (SPSS Inc., Chicago, IL, USA), and the Shapiro–Wilk test for normality was conducted in MATLAB 2019a (MathWorks, Natick, MA, USA).

SUPPLEMENTARY MATERIAL

See the supplementary material for Note 1. Temporal Evolution of Neural Signal Quality: Figs. S1 and S2 illustrate the MUA and LFP signals, respectively, recorded over 27 days from eight channels across four rats. The MUA SNR and trends indicate stable neural recordings during the baseline period (days 1–7) but a gradual decline afterward, suggesting possible signal degradation or electrode instability. Lower-frequency LFP signals remain more stable over time, whereas higher-frequency signals tend to degrade or fluctuate more across recording sessions. Table S1 presents the average MUA *SNR* values for each recording channel during the baseline period per implanted rat, along with the corresponding imputation thresholds. Channels with MUA *SNR* values below these thresholds in later recordings were classified as low-quality and imputed. Table S2 shows the LFP *Coh* values across six frequency bands (δ, θ, α, β, γ, and γ') during the baseline period implanted rat. These values were used to establish imputation thresholds, where channels with low coherence were identified for signal reconstruction. Table S3 lists the number of imputed channels per recording day for each rat, indicating the extent of signal degradation over time. The imputed channel ratio (%) was calculated as the percentage of channels that required imputation at each time point. Note 2. Algorithm Implementation of the kSIR Decoder: This section describes the mathematical framework of the kSIR decoder, detailing how neural features (MUA and LFP) were transformed into forelimb movement predictions. Equations outlining the slicing process, kernel function application, and regression model formulation are provided. Note 3. Imputing Low-Quality Neural Features Using Mean-imp and GMM-EM: This section describes the mathematical framework of the Mean-imp and GMM-EM methods. To compare imputation performance, low-quality neural data were also restored using Mean-imp and GMM-EM methods. The Mean-imp method used averaged values from high-quality channels, whereas GMM-EM estimated missing values based on probabilistic distributions. Note 4. Statistical Analysis for Determining Optimal kSIR Parameters: The selection of kernel width (σ) and regularization parameter (r) for the kSIR decoder was optimized using a two-way ANOVA, followed by post hoc Tukey's tests. Table S4 presents the decoding performance (RMSE) for different parameter pairs, and Fig. S3 visualizes statistical comparisons. Note 5. Correlation Between Neural Features and Forelimb Movement: Fig. S4 depicts the MIC analysis, which quantifies the relationship between neural activity and forelimb movement velocity over 27 days. MUA and high-frequency LFP bands (γ and γ') show the strongest correlation with movement but decline over time, suggesting signal degradation. Note 6. Comparison of CW-BLR, GMM-EM, and Mean-Imp Under Simulated Data Degradation: To evaluate decoding robustness, a simulation study artificially introduced missing neural data at varying imputation levels (12.5%–87.5%). CW-BLR demonstrated the highest decoding accuracy, maintaining stable performance up to 50% imputed channels, while GMM-EM and Mean-imp showed substantial performance degradation at lower thresholds (Fig. S5).

ACKNOWLEDGMENTS

This work was financially supported by the Taiwan National Science and Technology Council under Contract Nos. of NSTC-111-2321-B-A49-005, NSTC-113-2321-B-A49-016, NSTC-113-2622-8-A49-007-TE2, NSTC-113-2221-E-A49-015-MY2, and NSTC-114-2622-8-A49-008-TE2.

AUTHOR DECLARATIONS

Conflict of Interest

The authors have no conflicts to disclose.

Ethics Approval

Ethics approval for experiments reported in the submitted manuscript on animal or human subjects was granted. All experimental procedures were approved by the Taipei Medical University Institutional Animal Care and Use Committee (IACUC Approval number: LAC-2021-0207) for experimental animals.

Author Contributions

Yun-Ting Kuo: Conceptualization (equal); Data curation (equal); Investigation (equal); Methodology (equal); Software (lead); Validation (lead); Visualization (equal); Writing – original draft (equal). **Han-Lin Wang:** Conceptualization (supporting); Data curation (equal); Formal analysis (equal); Investigation (supporting); Software (supporting); Validation (equal); Visualization (supporting). **Bo-Wei Chen:** Data curation (supporting); Formal analysis (supporting); Methodology (supporting); Software (equal); Validation (equal); Visualization (equal); Writing – original draft (supporting). **Ching-Fu Wang:** Data curation (supporting); Formal analysis (supporting); Investigation (supporting); Project administration (supporting); Resources (supporting); Visualization (supporting); Writing – original draft (supporting). **Yu-Chun Lo:** Funding acquisition (equal); Investigation (equal); Project administration (equal); Resources (equal); Supervision (equal); Writing – original draft (equal). **Sheng-Huang Lin:** Funding acquisition (equal); Investigation (equal); Resources (equal); Supervision (equal); Validation (equal). **Po-Chuan Chen:** Data curation (supporting); Formal analysis (supporting); Methodology (supporting); Software (supporting); Validation (supporting); Visualization (supporting). **You-Yin Chen:** Conceptualization (lead); Data curation (equal); Funding acquisition (lead); Investigation (equal); Methodology (equal); Project administration (lead); Resources (lead); Supervision (lead); Writing – original draft (equal); Writing – review & editing (lead).

DATA AVAILABILITY

The data that support the findings of this study are available from the corresponding author upon reasonable request.

REFERENCES

[1]H. Petschenig *et al.*, "Classification of Whisker deflections from evoked responses in the somatosensory barrel cortex with spiking neural networks," Front. Neurosci. **16**, 838054 (2022).
[2]T. V. Ness, M. W. Remme, and G. T. Einevoll, "Active subthreshold dendritic conductances shape the local field potential," J. Physiol. **594**(13), 3809–3825 (2016).
[3]Y. Murayama *et al.*, "Relationship between neural and hemodynamic signals during spontaneous activity studied with temporal kernel CCA," Magn. Reson. Imaging **28**(8), 1095–1103 (2010).
[4]A. Jackson and T. M. Hall, "Decoding local field potentials for neural interfaces," IEEE Trans. Neural Syst. Rehabil. Eng. **25**(10), 1705–1714 (2017).
[5]M. Esghaei, M. R. Daliri, and S. Treue, "Attention decouples action potentials from the phase of local field potentials in macaque visual cortical area MT," BMC Biol. **16**, 1–13 (2018).
[6]H. Farooqi, J. L. Vitek, and D. E. Sanabria, "Deep brain stimulation pulse sequences to optimally modulate frequency-specific neural activity," J. Neural Eng. **21**, 036045 (2024).
[7]B. Sun *et al.*, "Compressed sensing of large-scale local field potentials using adaptive sparsity analysis and non-convex optimization," J. Neural Eng. **18**(2), 026007 (2021).
[8]N. T. Tasneem *et al.*, "A fully integrated 1.13 NEF 32-channel neural recording SoC with 12.5 pJ/pulse IR-UWB wireless transmission for brain machine interfaces," IEEE Access **11**, 109294–109306 (2023).
[9]N. Ahmadi, T. G. Constandinou, and C.-S. Bouganis, "Inferring entire spiking activity from local field potentials," Sci. Rep. **11**(1), 19045 (2021).
[10]F. Zhang *et al.*, "A machine learning-based multiple imputation method for the health and aging brain study–health disparities," Informatics **10**, 77 (2023).
[11]X. Qian *et al.*, "A platform for long-term monitoring the deep brain rhythms," Biomed. Phys. Eng. Express **3**(1), 015009 (2017).
[12]J. Zhuang *et al.*, "Decoding 3-D reach and grasp kinematics from high-frequency local field potentials in primate primary motor cortex," IEEE Trans. Biomed. Eng. **57**(7), 1774–1784 (2010).
[13]M. Gwilt, M. Bauer, and T. Bast, "Frequency-and state-dependent effects of hippocampal neural disinhibition on hippocampal local field potential oscillations in anesthetized rats," Hippocampus **30**(10), 1021–1043 (2020).
[14]W.-J. Pan *et al.*, "Infraslow LFP correlates to resting-state fMRI BOLD signals," Neuroimage **74**, 288–297 (2013).
[15]A. Mazzoni *et al.*, "Cortical dynamics during naturalistic sensory stimulations: Experiments and models," J. Physiol. **105**(1–3), 2–15 (2011).
[16]H. Sepehrian and B. Gosselin, "A low-power current-reuse dual-band analog front-end for multi-channel neural signal recording," in *36th Annual International Conference of the IEEE Engineering in Medicine and Biology Society* (IEEE, 2014).
[17]X. Qian *et al.*, "Implanted rechargeable electroencephalography (EEG) device," Electron. Lett. **50**(20), 1419–1421 (2014).
[18]J.-M. Braun *et al.*, "A brain machine interface framework for exploring proactive control of smart environments," Sci. Rep. **14**(1), 11054 (2024).
[19]S.-H. Yang, C.-J. Huang, and J.-S. Huang, "Increasing robustness of intracortical brain-computer interfaces for recording condition changes via data augmentation," Comput. Methods Programs Biomed. **251**, 108208 (2024).
[20]M. B. Badsha *et al.*, "Imputation of single-cell gene expression with an autoencoder neural network," Quant. Biol. **8**(1), 78–94 (2020).
[21]K. Getz, R. A. Hubbard, and K. A. Linn, "Performance of multiple imputation using modern machine learning methods in electronic health records data," Epidemiology **34**(2), 206–215 (2023).
[22]B. K. Beaulieu-Jones, J. H. Moore, and P.-A. Consortium, "*Missing data imputation in the electronic health record using deeply learned autoencoders*," in *Pacific Symposium on Biocomputing 2017* (World Scientific, 2017).
[23]C.-H. Kuo *et al.*, "Decoding micro-electrocorticographic signals by using explainable 3D convolutional neural network to predict finger movements," J. Neurosci. Methods **411**, 110251 (2024).
[24]C. Pandarinath and S. J. Bensmaia, "The science and engineering behind sensitized brain-controlled bionic hands," Physiol. Rev. **102**(2), 551–604 (2022).
[25]X. Li *et al.*, "Neural correlates of fine motor grasping skills: Longitudinal insights into motor cortex activation using fNIRS," Brain Behavior **14**(1), e3383 (2024).
[26]A. K. Bansal *et al.*, "Decoding 3D reach and grasp from hybrid signals in motor and premotor cortices: Spikes, multiunit activity, and local field potentials," J. Neurophysiol. **107**(5), 1337–1355 (2012).
[27]M. Kashefi and M. R. Daliri, "A stack LSTM structure for decoding continuous force from local field potential signal of primary motor cortex (M1)," BMC Bioinf. **22**(1), 1–19 (2021).
[28]S. D. Muthukumaraswamy, "Functional properties of human primary motor cortex gamma oscillations," J. Neurophysiol. **104**(5), 2873–2885 (2010).
[29]D. Cheyne *et al.*, "Self-paced movements induce high-frequency gamma oscillations in primary motor cortex," Neuroimage **42**(1), 332–342 (2008).
[30]C. Tallon-Baudry and O. Bertrand, "Oscillatory gamma activity in humans and its role in object representation," Trends Cognit. Sci. **3**(4), 151–162 (1999).
[31]R. Lemon and J. Van Der Burg, "Short-latency peripheral inputs to thalamic neurones projecting to the motor cortex in the monkey," Exp. Brain Res. **36**(3), 445–462 (1979).
[32]J. Marsden *et al.*, "Organization of cortical activities related to movement in humans," J. Neurosci. **20**(6), 2307–2314 (2000).
[33]J. Liu and W. T. Newsome, "Local field potential in cortical area MT: Stimulus tuning and behavioral correlations," J. Neurosci. **26**(30), 7779–7790 (2006).
[34]J.-E. W. Skaar *et al.*, "Estimation of neural network model parameters from local field potentials (LFPs)," PLoS Comput. Biol. **16**(3), e1007725 (2020).
[35]G. Buzsáki, C. A. Anastassiou, and C. Koch, "The origin of extracellular fields and currents—EEG, ECoG, LFP and spikes," Nat. Rev. Neurosci. **13**(6), 407–420 (2012).
[36]K. Bhavna *et al.*, "Explainable deep-learning framework: Decoding brain states and prediction of individual performance in false-belief task at early childhood stage," Front. Neuroinf. **18**, 1392661 (2024).
[37]V. N. Murthy and E. E. Fetz, "Coherent 25-to 35-Hz oscillations in the sensorimotor cortex of awake behaving monkeys," Proc. Natl. Acad. Sci. U. S. A. **89**(12), 5670–5674 (1992).
[38]A. Jahani *et al.*, "Spatially distinct beta-band activities reflect implicit sensorimotor adaptation and explicit re-aiming strategy," J. Neurosci. **40**(12), 2498–2509 (2020).
[39]D. Borra *et al.*, "Modulations of cortical power and connectivity in alpha and beta bands during the preparation of reaching movements," Sensors **23**(7), 3530 (2023).
[40]R. Sharma and S. Nadkarni, "Biophysical basis of alpha rhythm disruption in Alzheimer's disease," eNeuro **7**(2), ENEURO.0293-19.2020 (2020).
[41]C. Cao *et al.*, "Low-beta versus high-beta band cortico-subcortical coherence in movement inhibition and expectation," Neurobiol. Disease **201**, 106689 (2024).
[42]E. Santarnecchi *et al.*, "High-gamma oscillations in the motor cortex during visuo-motor coordination: A tACS interferential study," Brain Res. Bull. **131**, 47–54 (2017).
[43]P. Berens *et al.*, "Comparing the feature selectivity of the gamma-band of the local field potential and the underlying spiking activity in primate visual cortex," Front. Syst. Neurosci. **2**, 258 (2008).
[44]A. Fernandez-Ruiz *et al.*, "Over and above frequency: Gamma oscillations as units of neural circuit operations," Neuron **111**(7), 936–953 (2023).
[45]I. Leunissen *et al.*, "Effects of beta-band and gamma-band rhythmic stimulation on motor inhibition," IScience **25**(5), 104338 (2022).
[46]L. L. Colgin and E. I. Moser, "Gamma oscillations in the hippocampus," Physiology **25**(5), 319–329 (2010).
[47]J. Lourenço, F. Koukouli, and A. Bacci, "Synaptic inhibition in the neocortex: Orchestration and computation through canonical circuits and variations on the theme," Cortex **132**, 258–280 (2020).
[48]H. Tan *et al.*, "Decoding gripping force based on local field potentials recorded from subthalamic nucleus in humans," eLife **5**, e19089 (2016).
[49]E. Tatti *et al.*, "Modulation of gamma spectral amplitude and connectivity during reaching predicts peak velocity and movement duration," Front. Neurosci. **16**, 836703 (2022).
[50]Y. Inoue *et al.*, "Decoding arm speed during reaching," Nat. Commun. **9**(1), 5243 (2018).
[51]M.-K. Kim, J.-W. Sohn, and S.-P. Kim, "Decoding kinematic information from primary motor cortex ensemble activities using a deep canonical correlation analysis," Front. Neurosci. **14**, 509364 (2020).
[52]P. J. Rousche and R. A. Normann, "Chronic recording capability of the Utah Intracortical Electrode Array in cat sensory cortex," J. Neurosci. Methods **82**(1), 1–15 (1998).

[53]J. C. Williams, R. L. Rennaker, and D. R. Kipke, "Long-term neural recording characteristics of wire microelectrode arrays implanted in cerebral cortex," Brain Res. Protoc. **4**(3), 303–313 (1999).
[54]E. J. Hwang and R. A. Andersen, "The utility of multichannel local field potentials for brain–machine interfaces," J. Neural Eng. **10**(4), 046005 (2013).
[55]N. Ahmadi, T. G. Constandinou, and C.-S. Bouganis, "End-to-end hand kinematic decoding from lfps using temporal convolutional network," in *IEEE Biomedical Circuits and Systems Conference (BioCAS)* (IEEE, 2019).
[56]Y. Dong *et al.*, "Neural decoding for intracortical brain–computer interfaces," Cyborg Bionic Syst. **4**, 0044 (2023).
[57]J. O. Usoro *et al.*, "Chronic stability of local field potentials from standard and modified Blackrock microelectrode arrays implanted in the rat motor cortex," Biomed. Phys. Eng. Express **5**(6), 065017 (2019).
[58]E. N. Jeakle *et al.*, "Chronic stability of local field potentials using amorphous silicon carbide microelectrode arrays implanted in the rat motor cortex," Micromachines **14**(3), 680 (2023).
[59]T. D. Kozai *et al.*, "Comprehensive chronic laminar single-unit, multi-unit, and local field potential recording performance with planar single shank electrode arrays," J. Neurosci. Methods **242**, 15–40 (2015).
[60]S. Liu *et al.*, "A nanowell-based MoS2 neuroelectrode for high-sensitivity neural recording," Iscience **27**(10), 110949 (2024).
[61]A. Ciarleglio, E. Petkova, and O. Harel, "Elucidating age and sex-dependent association between frontal EEG asymmetry and depression: An application of multiple imputation in functional regression," J. Am. Stat. Assoc. **117**(537), 12–26 (2022).
[62]H. Scherberger, M. R. Jarvis, and R. A. Andersen, "Cortical local field potential encodes movement intentions in the posterior parietal cortex," Neuron **46**(2), 347–354 (2005).
[63]M. Cubillos, S. Wøhlk, and J. N. Wulff, "A bi-objective k-nearest-neighbors-based imputation method for multilevel data," Expert Syst. Appl. **204**, 117298 (2022).
[64]D. M. Rodgers *et al.*, "A multiple imputation approach for handling missing data in classification and regression trees," J. Behav. Sci. **1**(1), 127–153 (2021).
[65]S. Lee, V. Periwal, and J. Jo, "Inference of stochastic time series with missing data," Phys. Rev. E **104**(2), 024119 (2021).
[66]S. F. Nielsen, "The stochastic EM algorithm: Estimation and asymptotic results," Bernoulli **6**, 457–489 (2000).
[67]A. Katsevich and A. S. Bandeira, "Likelihood maximization and moment matching in low SNR Gaussian mixture models," Commun. Pure Appl. Math. **76**(4), 788–842 (2023).
[68]L. Malan *et al.*, "Missing data imputation via the expectation-maximization algorithm can improve principal component analysis aimed at deriving biomarker profiles and dietary patterns," Nutr. Res. **75**, 67–76 (2020).
[69]C. K. Enders, "Using the expectation maximization algorithm to estimate coefficient alpha for scales with item-level missing data," Psychol. Methods **8**(3), 322 (2003).
[70]V. Borisov *et al.*, "Deep neural networks and tabular data: A survey," IEEE Trans. Neural Networks Learn. Syst. **35**(6), 7499–7519 (2022).
[71]A. Khorasani, V. Shalchyan, and M. R. Daliri, "Adaptive artifact removal from intracortical channels for accurate decoding of a force signal in freely moving rats," Front. Neurosci. **13**, 350 (2019).
[72]L. Cappelletti *et al.*, "Complex data imputation by auto-encoders and convolutional neural networks—A case study on genome gap-filling," Computers **9**(2), 37 (2020).
[73]A. Ghanbari *et al.*, "Modeling stimulus-dependent variability improves decoding of population neural responses," J. Neural Eng. **16**(6), 066018 (2019).
[74]G. Sharma *et al.*, "Using an artificial neural bypass to restore cortical control of rhythmic movements in a human with quadriplegia," Sci. Rep. **6**(1), 33807 (2016).
[75]V. Rostami *et al.*, "Spiking attractor model of motor cortex explains modulation of neural and behavioral variability by prior target information," Nat. Commun. **15**(1), 6304 (2024).
[76]K. Junaid *et al.*, "How much missing data is too much to impute for longitudinal health indicators? A preliminary guideline for the choice of the extent of missing proportion to impute with multiple imputation by chained equations," Popul. Health Metrics **23**(1), 2 (2025).
[77]G. Basalyga and E. Salinas, "When response variability increases neural network robustness to synaptic noise," Neural Comput. **18**(6), 1349–1379 (2006).
[78]S. Reich and R. Rosenbaum, "The impact of short term synaptic depression and stochastic vesicle dynamics on neuronal variability," J. Comput. Neurosci. **35**(1), 39–53 (2013).
[79]F. Duan *et al.*, "Decoding premovement patterns with task-related component analysis," Cogn. Comput. **13**, 1389–1405 (2021).
[80]H.-C. Lin *et al.*, "Central thalamic deep-brain stimulation alters striatal-thalamic connectivity in cognitive neural behavior," Front. Neural Circuits **9**, 87 (2016).
[81]H.-L. Wang *et al.*, "Enhancing prediction of forelimb movement trajectory through a calibrating-feedback paradigm incorporating rat primary motor and agranular cortical ensemble activity in the goal-directed reaching task," Int. J. Neural Syst. **33**(10), 2350051 (2023).
[82]V. Tsytsarev *et al.*, "Imaging cortical electrical stimulation *in vivo*: Fast intrinsic optical signal versus voltage-sensitive dyes," Opt. Lett. **33**(9), 1032–1034 (2008).
[83]K. Kumaravelu and W. M. Grill, "Neural mechanisms of the temporal response of cortical neurons to intracortical microstimulation," Brain Stimul. **17**(2), 365–381 (2024).
[84]Q. Tang *et al.*, "*In vivo* mesoscopic voltage-sensitive dye imaging of brain activation," Sci. Rep. **6**(1), 25269 (2016).
[85]S.-H. Yang *et al.*, "Inhibition of long-term variability in decoding forelimb trajectory using evolutionary neural networks with error-correction learning," Front. Comput. Neurosci. **14**, 22 (2020).
[86]S.-H. Yang *et al.*, "A sliced inverse regression (SIR) decoding the forelimb movement from neuronal spikes in the rat motor cortex," Front. Neurosci. **10**, 556 (2016).
[87]D. Ramanathan, J. M. Conner, and M. H. Tuszynski, "A form of motor cortical plasticity that correlates with recovery of function after brain injury," Proc. Natl. Acad. Sci. U. S. A. **103**(30), 11370–11375 (2006).
[88]A. R. Brown and G. C. Teskey, "Motor cortex is functionally organized as a set of spatially distinct representations for complex movements," J. Neurosci. **34**(41), 13574–13585 (2014).
[89]C. Gallego-Carracedo *et al.*, "Local field potentials reflect cortical population dynamics in a region-specific and frequency-dependent manner," Elife **11**, e73155 (2022).
[90]S. D. Stavisky *et al.*, "A high performing brain–machine interface driven by low-frequency local field potentials alone and together with spikes," J. Neural Eng. **12**(3), 036009 (2015).
[91]G. Sharma *et al.*, "Time stability and coherence analysis of multiunit, single-unit and local field potential neuronal signals in chronically implanted brain electrodes," Bioelectron. Med. **2**(1), 63–71 (2015).
[92]H.-M. Wu, "Kernel sliced inverse regression with applications to classification," J. Comput. Graph. Stat. **17**(3), 590–610 (2008).
[93]Q. Wu, F. Liang, and S. Mukherjee, *Regularized Sliced Inverse Regression for Kernel Models* (Citeseer, 2007).
[94]H. Tan *et al.*, "Decoding voluntary movements and postural tremor based on thalamic LFPs as a basis for closed-loop stimulation for essential tremor," Brain Stimul. **12**(4), 858–867 (2019).
[95]A. Khorasani *et al.*, "Continuous force decoding from local field potentials of the primary motor cortex in freely moving rats," Sci. Rep. **6**(1), 35238 (2016).
[96]T. Liang *et al.*, "Time-frequency maximal information coefficient method and its application to functional corticomuscular coupling," IEEE Trans. Neural Syst. Rehabil. Eng. **28**(11), 2515–2524 (2020).
[97]J. Bhattacharya, E. Pereda, and C. Ioannou, "Functional associations at global brain level during perception of an auditory illusion by applying maximal information coefficient," Physica A **491**, 708–715 (2018).